Topological braiding and virtual particles on the cell membrane

Jinghui Liu[a], Jan F. Totz[b,c], Pearson W. Miller[d], Alasdair D. Hastewell[b], Yu-Chen Chao[a,e], Jörn Dunkel[b,1], and Nikta Fakhri[a,1]

[a]Department of Physics, Massachusetts Institute of Technology, Cambridge, MA 02139; [b]Department of Mathematics, Massachusetts Institute of Technology, Cambridge, MA 02139; [c]Department of Mechanical Engineering, Massachusetts Institute of Technology, Cambridge, MA 02139; [d]Center for Computational Biology, Flatiron Institute, Simons Foundation, New York, NY 10010; and [e]School of Engineering and Applied Sciences, Harvard University, Cambridge, MA 02138

Edited by David A. Weitz, Harvard University, Cambridge, MA, and approved July 13, 2021 (received for review March 3, 2021)

Braiding of topological structures in complex matter fields provides a robust framework for encoding and processing information, and it has been extensively studied in the context of topological quantum computation. In living systems, topological defects are crucial for the localization and organization of biochemical signaling waves, but their braiding dynamics remain unexplored. Here, we show that the spiral wave cores, which organize the Rho-GTP protein signaling dynamics and force generation on the membrane of starfish egg cells, undergo spontaneous braiding dynamics. Experimentally measured world line braiding exponents and topological entropy correlate with cellular activity and agree with predictions from a generic field theory. Our analysis further reveals the creation and annihilation of virtual quasi-particle excitations during defect scattering events, suggesting phenomenological parallels between quantum and living matter.

braiding | topological defects | biochemical signaling waves | virtual particles | information transport

Braiding confers remarkable robustness to static and dynamic structures, from plaited hair and fabrics (1) to the entangled world lines of classical (2) and quantum particles (3). Stabilized by an inherent topological protection, braided threads, ropes, and wires have long been used to transmit forces and shield signals (4). Over the last decade, dynamic braiding processes (5–7) have attracted major interest in soft matter (8, 9) and quantum physics (3) as promising candidates for robust information storage and processing (10, 11). A widely studied application is topological quantum algorithms that perform computations by braiding the world lines of two-dimensional (2D) quasiparticle excitations (3, 10, 11). Of similar importance to information processing in living systems—albeit much less well understood—are the braiding dynamics of chemical spiral wave signals on cell membranes, which control a wide range of developmental and physiological functions, including cell division (12), cardiac rhythm (13–16), and brain activity (17). These spiral waves belong to a rapidly expanding class of recently discovered biological phenomena (18, 19) in which topological structures serve as robust organizers of essential life processes.

Similar to quantum states, biochemical spiral wave patterns can be described by complex wave functions (20), with spiral cores acting as topologically protected 2D quasiparticles (21). Although modern live-cell imaging now enables the direct observation of membrane spiral waves (22), their braiding dynamics have remained unexplored due to insufficient spatiotemporal resolution. Identifying the dynamic similarities and differences between 2D biochemical and quantum excitations poses a theoretically and practically relevant challenge, since optogenetic advances (23, 24) promise unprecedented control over cell signaling and hence biological computation. A particularly interesting open question in this context is whether fundamental quantum mechanical particle–particle interactions, symmetries (25), and scattering phenomena find counterparts in biological signaling processes. Our combined experimental and theoretical results below show that the self-braiding events of biochemical spiral wave cores on the cell membranes can exhibit virtual particle pair creation and annihilation and bosonic exchange symmetry, revealing profound parallels between defect dynamics and information transport in living and quantum matter.

Driven by recent experimental progress (18, 22, 26–28), the exploration of topological defects in synthetic and natural active matter has become a rapidly expanding area of research (29–38). In living systems, energy conversion of ATP at the microscale leads to the emergence of complex biochemical and biophysical signaling patterns at the mesoscale and macroscale (22, 27, 39). Such nonequilibrium patterns often display rich topological textures and dynamics (32, 33, 40, 41), arising from the defects' self-propulsion (29) and interactions (30, 31). Owing to their robustness and slow dynamics, topological excitations can act as stabilizers and organizers of active force generation (18), biological functions (19), and information flows. Recent work determined the topological entropy associated with the braiding of defects in active nematic liquid crystals (37). By contrast, the relation between spontaneous topological defect braiding and information loss in

Significance

Topological defects are robust particle-like structures that essentially determine the mechanics and dynamics of physical and biological matter. Examples range from vortices in quantum superfluids to the cores of spiral wave patterns in the brain. In biological systems, such defects play important roles as organizers of biochemical signaling patterns, cellular forces, and even cell death. Combining direct experimental observations with mathematical modeling and chemical perturbations, we investigated the dynamics of spiral wave defects on the surfaces of starfish egg cells. Our quantitative analysis showed that these defects exhibit complex braiding, pair creation, and annihilation dynamics, in agreement with predictions from a generic continuum theory. More broadly, these results suggest interesting parallels between information transport in living and quantum systems.

Author contributions: J.D. and N.F. designed research; J.L., J.F.T., P.W.M., A.D.H., and Y.-C.C. performed research; J.L., J.F.T., P.W.M., and A.D.H. contributed new reagents/analytic tools; J.L., J.F.T., and A.D.H. analyzed data; and J.L., J.F.T., P.W.M., A.D.H., Y.-C.C., J.D., and N.F. wrote the paper.

The authors declare no competing interest.

This article is a PNAS Direct Submission.

[1]To whom correspondence may be addressed. Email: dunkel@mit.edu or fakhri@mit.edu.

This article contains supporting information online at https://www.pnas.org/lookup/suppl/doi:10.1073/pnas.2104191118/-/DCSupplemental.

Published August 20, 2021.

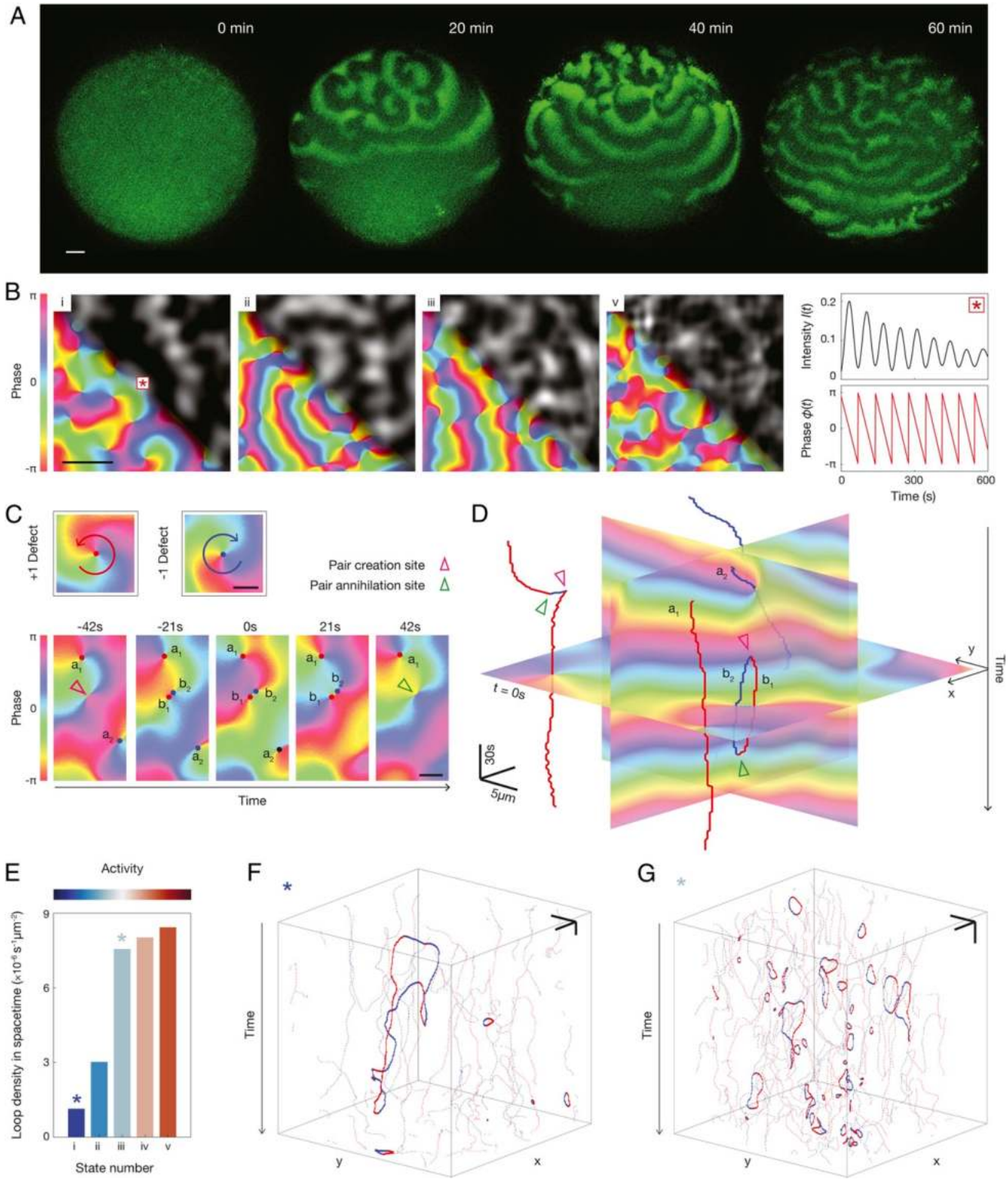

Fig. 1. Direct measurement of defect world line dynamics during membrane signaling wave propagation. (*A*) Time evolution of chemical Rho signaling wave patterns on the starfish oocyte from a homogeneous initial state to a quasi-steady state exhibiting turbulent spiral patterns. Snapshots show maximal intensity projections of three near-membrane Z-stack confocal slices spanning 5 μm (Movie S1). (Scale bar: 40 μm.) (*B*) Quasi-steady wave patterns ($t > 60$ min) of Rho-GTP intensity field from four starfish egg cells, aligned with phase fields reconstructed from oscillations in pixel fluorescence intensity signal (*Right*). (Scale bar: 20 μm.) Five wave propagation states on five different egg cells were analyzed in total (Movies S2–S6). (*C*) The reconstructed phase fields harbor topological defects of winding number +1 (red, counterclockwise rotating spiral core) and −1 (blue, clockwise rotating spiral core) (*Upper*). Time-lapse snapshots of localized creation (annihilation) events that produce (destroy) oppositely charged defects in pairs (*Lower*). (Scale bar: 5 μm.) (*D*) World line representation of topological defects embedded in 2+1-dimensional phase field. The time-lapse snapshots in *C* correspond to formation of the simple space−time loop in *D*. (Scale bars: 5 μm; 30 s [vertical] [Movie S7]). (*E*) Loop density characterizes signaling waves from five different oocytes (states i to v) varying in cellular activity. Asterisks annotate the lower-activity and higher-activity state i and iii, as presented next in *F* and *G*. (*F*) Space−time defect loops from experimental wave state i (lower activity). (Scale bars: 10 μm; 90 s [vertical]). (*G*) Space−time defect loops from experimental wave state iii (higher activity). (Scale bars: 10 μm; 90 s [vertical]).

cell membrane signaling processes (22) has remained relatively unexplored.

To investigate the braiding dynamics of biochemical spiral waves in living cells, we compared here experimental observations of Rho-GTP activation waves on starfish oocyte membranes (22) with predictions of a generic continuum theory (20). Rho-GTP is a highly conserved signaling protein pivotal in regulating cellular division (42) and mechanics (43) across a wide variety of eukaryotic species (44). Since the biological functions of Rho-GTP have been widely investigated previously (45), we focused here on the topological characterization of the biochemical signaling dynamics through braiding analysis of defect world lines and entropic information measures, to identify similarities and differences with wave propagation and particle scattering dynamics in quantum systems. Overcoming previous observational and algorithmic limitations, we achieved the spatiotemporal resolution required for dynamical analysis by combining in vivo imaging with spectral signal representation, quantitative mathematical modeling, and large-scale computational parameter estimations (*Materials and Methods*) (46).

Results

Topological Defect Dynamics in Rho-GTP Signaling Patterns. To visualize the self-organized Rho-GTP wave patterns on the membrane of the oocytes (45), we used the enhanced green fluorescent protein/rhotekin GTPase binding domain (eGFP-rGBD) biosensor (Fig. 1*A* and *SI Appendix*, Fig. S1 and Movie S1). Different steady-state patterns of Rho-GTP were induced by a systematic increase of the GEF (guanine exchange factor) responsible for activating Rho-GTP (states i to v) (39). Rho-GTP waves maintained constant oscillatory periods within all observed nonequilibrium steady states with different cellular activity (22) (Movies S2–S6), enabling the reconstruction of spatiotemporal phase fields (Fig. 1*B* and *SI Appendix*, Fig. S2 and *Materials and Methods*). Topological defects in the phase field are singular points with winding number $+1$ or -1 corresponding to counterclockwise or clockwise rotating centers of propagating spiral waves (Fig. 1*C*). These phase defects are created and annihilated in pairs, conserving the total topological charge (Fig. 1*C*). By tracking the $2+1$-dimensional world lines of both defect types, we observed complex creation, annihilation, and braiding dynamics (Fig. 1*D*), similar to those in Bose–Einstein condensates (46, 47) (Movie S7). Closed space–time loops (*SI Appendix*, Fig. S3) reflect successive defect pair creation and annihilation events. Rho-GTP spiral waves from the five observed oocytes exhibited varying densities of space–time defect loops, reflecting differences in cellular activity (Fig. 1*E*). Despite such quantitative variations, all signaling patterns displayed a wide range of loop structures and sizes (Fig. 1 *F* and *G* and *SI Appendix*, Fig. S3). Steady-state spiral waves of low-activity oocytes (Fig. 1*F*) exhibited a lower loop density compared with high-activity cells (Fig. 1*G*). To confirm the link between cellular activity and defect loop statistics,

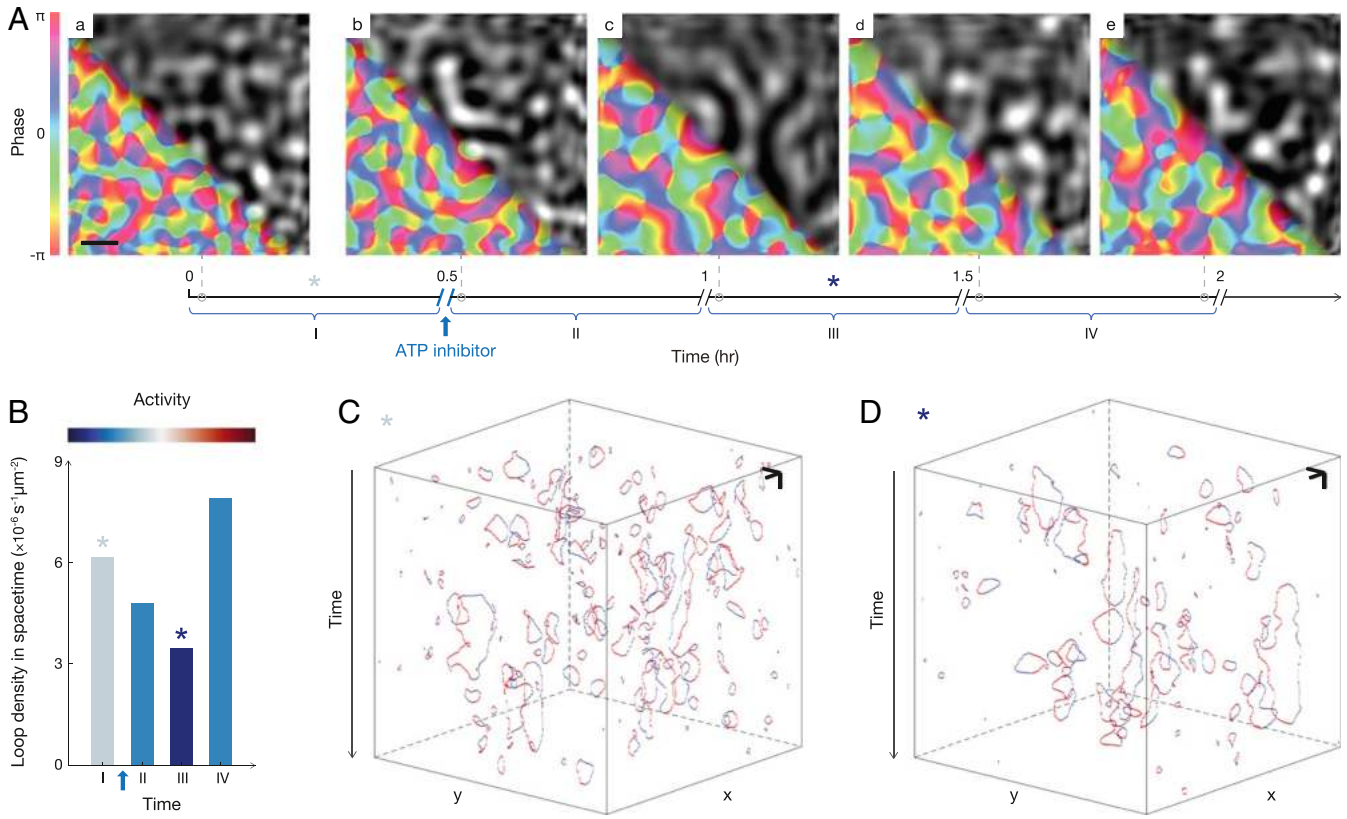

Fig. 2. ATP depletion induces structural changes in the membrane signaling patterns and reduces the frequency of topological defect creation and annihilation events. (*A*) Time evolution of Rho-GTP intensity field and phase field from a starfish egg cell treated with ATP depletion drug sodium azide (*Materials and Methods* and Movie S8). Videos I through IV in Movie S8 each has a duration of 30 min and were taken sequentially, separated by short (<3 min) intervals in between. The drug treatment was performed after video I and before the start of video II. (Scale bars: 20 μm.) Asterisks denote the pretreatment video I and posttreatment video III, as presented next in *B*–*D*. (*B*) Loop density as a function of time showing a transient drop in cellular activity in response to the ATP depletion treatment. (*C*) Space–time defect loops before ATP depletion recorded during phase I in *A*. (Scale bars: 10 μm; 90 s [vertical]). (*D*) After ATP depletion (phase III in *A*), the density of space–time defect loops decreases significantly, reflecting the reduction of cellular activity. (Scale bars: 10 μm; 90 s [vertical]).

we performed additional experiments, in which starfish oocytes exhibiting steady-state wave patterns were perturbed with the ATP-depleting drug sodium azide (*Materials and Methods* and Fig. 2). After exposure to the drug, the Rho-GTP concentration patterns (Movie S8) and their associated phase fields displayed visible structural and dynamical changes (Fig. 2*A*): Over a period of ∼1 h, the space–time loop densities decreased, reflecting the decrease in cellular activity, before eventually returning to preperturbed levels (Fig. 2 *B–D* and *SI Appendix*, Fig. S3). These observations are consistent with the previous measurements for steady-state cells (Fig. 1 *B* and *E–G*), supporting the hypothesis that cellular activity and topological defect dynamics are linked.

Defect Braiding Dynamics. In addition to short-lived loops which dominate at high activity, low-activity states (Fig. 1 *B*, *i–iii*) exhibit a large number of long-lived defect world lines that undergo spontaneous braiding dynamics (Fig. 3*A*). Space–time braiding of spiral cores is indicative of chaotic dynamics of the Rho-GTP signaling patterns. To quantify the associated topological entropy increase, we classified braiding events by adopting the reduced Burau matrix representation of the n-particle braid group (48). To this end, we first identified elementary braiding events from the crossing of projected world lines (Fig. 3*A*). Each clockwise or counterclockwise braiding event n is then represented by a $(n-1)\times(n-1)$ matrix $\sigma^{(n)}\in\{\sigma_i,\sigma_i^{-1}\}$, where the σ_i are the generators of Burau representation (*Materials and Methods*). Accordingly, a sequence of $n=1,\ldots,N$ successive braiding events is encoded by the matrix product $\Sigma^{(N)}=\sigma^{(N)}\sigma^{(N-1)}\ldots\sigma^{(1)}$ of the corresponding elementary generators (2). The largest eigenvalue Λ of the braid matrix $\Sigma^{(N)}$, known as the braiding factor, determines the braiding exponent $\lambda=(1/t)\log\Lambda$, which measures the growth rate of the topological entropy in chaotic systems (2).

Braiding Exponents and Topological Entropy. To calculate the braiding exponents λ from our experimental data (6), we constructed a library of long-lived $+1$ and -1 defect world lines for the low-activity signaling states i, ii, and iii (Fig. 3*A* and *Materials and Methods*). Braiding exponents for different defect numbers were then computed and averaged across subgroups of world lines bootstrapped from the library (*SI Appendix*, Figs. S4 and S5 and *Materials and Methods*). Our evaluation

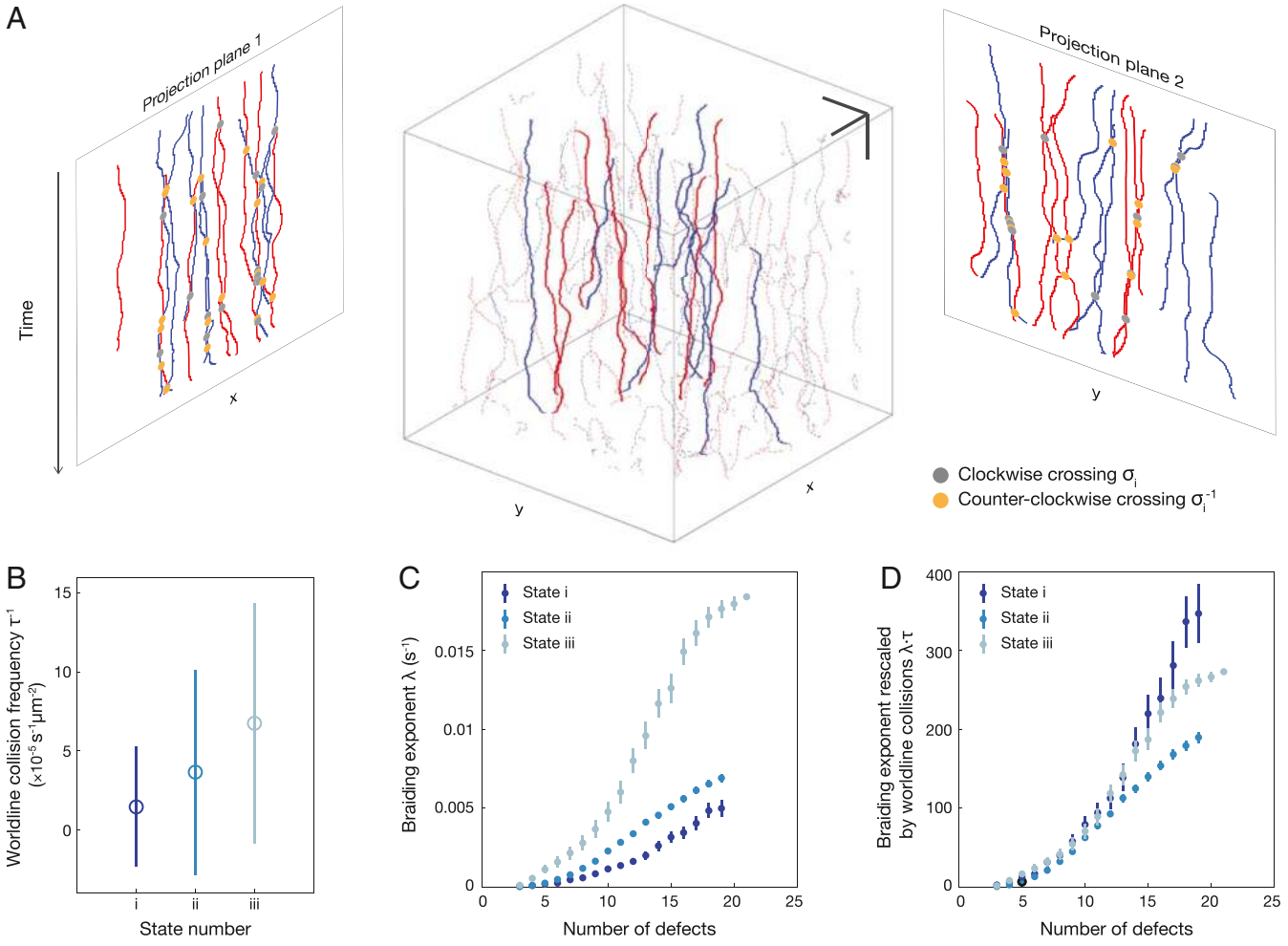

Fig. 3. Spontaneous braiding of topological defects and world line collisions during cell signaling. (*A*) Representative selection of braided defect world lines from low-activity state i. Braiding dynamics are quantified by multiplying braiding operators (σ_i, σ_i^{-1}) and averaging over a collection of projected world line cross-overs (*Materials and Methods* and *SI Appendix*, Fig. S4). (Scale bars: 20 μm; 240 s [vertical]). (*B*) World line collision (defect pair creation and annihilation) frequencies per unit area for states i, ii, and iii exhibit a sequential rise. Error bars represent SD throughout time. (*C*) Measured braiding exponents as a function of total defect number exhibit a sequential rise in magnitude with increasing activities from states i to iii. Error bars represent SE across bootstrap samples. (*D*) Braiding exponents from *C* collapse when rescaled by the world line collision frequencies. Error bars represent SE across bootstrap samples.

of world line collision frequencies reveals different time scales of cellular activities across signaling wave states (Fig. 3*B*). The estimated braiding exponents support the hypothesis that topological entropy increases faster at higher cellular activity (Fig. 3*C*). When rescaled by the world line collision frequencies τ^{-1}, the braiding exponents collapse onto a single curve (Fig. 3*D*). This result presents a direct link between the spontaneous topological braiding of spiral defects and information loss in the cellular signaling waves.

Discussion

Quantitative Mapping to a Complex Ginzburg–Landau Theory. To understand whether the above results translate to a broader class of biochemical signaling systems, we compared the experimentally observed loop and braiding dynamics with predictions from a generic spiral wave theory (20). We simulated a complex Ginzburg–Landau (CGL) continuum model (20, 49) with tunable levels of activity (Fig. 4*A* and *SI Appendix*, Fig. S6). The CGL theory describes a general class of nonlinear waves capable of embedding spiral cores, for which effective diffusion and reaction parameters can be systematically derived as combinations of constants from a multispecies reaction–diffusion system (*SI Appendix*, Figs. S7 and S8 and *Materials and Methods*). By tuning the reaction parameter in the CGL model, we were able to quantitatively match the CGL phase field dynamics to the oocyte states i, ii, and iii in both space (Fig. 4*A* and *SI Appendix*, Fig. S9) and time (Fig. 4 *B* and *C*, Movie S9, and *Materials and Methods*). Detailed braiding analysis of the space–time defect dynamics of CGL states confirmed that higher-activity states show faster topological entropy growth (Fig. 4*D*). In agreement with our experimental observations, the braiding exponents collapse when rescaled by the world line collision frequencies (Fig. 4*E*). Taken together, these results support the conclusion that essential aspects of wave-mediated information processing on the oocyte membrane can be modeled and studied within a generic CGL theory framework.

Virtual Quasi-particle Excitations on the Cell Membrane. Macroscopic information loss in spiral wave signaling patterns results from the microscopic interactions between the defect cores. Future efforts to control biochemical membrane signaling through optogenetic intervention will thus require a detailed understanding of microscopic defect scattering events. We therefore applied our analysis framework to study the previously inaccessible short-range defect scattering dynamics. While two colliding opposite-sign spiral cores tend to annihilate, a pair of interacting same-sign spiral cores can exhibit intricate dynamics (Fig. 5). In addition to basic pair-braiding dynamics (Fig. 5*A* and Movie S10), our data revealed scattering events during which short-lived "virtual" particles were created (Fig. 5 *B* and *C*). Such virtual particles annihilated either mutually (Fig. 4*B* and Movie S10) or by recombination with one of the original defects (Fig. 5*C* and Movie S10). These biochemical scattering events have known counterparts in quantum systems (50), and all of them can also be identified in the corresponding CGL wave states (Fig. 5, *Lower*). Another interesting parallel with quantum systems relates to the pair exchange symmetry when two equal-sign spiral defects exchange positions through braiding. In the case of two identical quantum particles, the global phase shift acquired

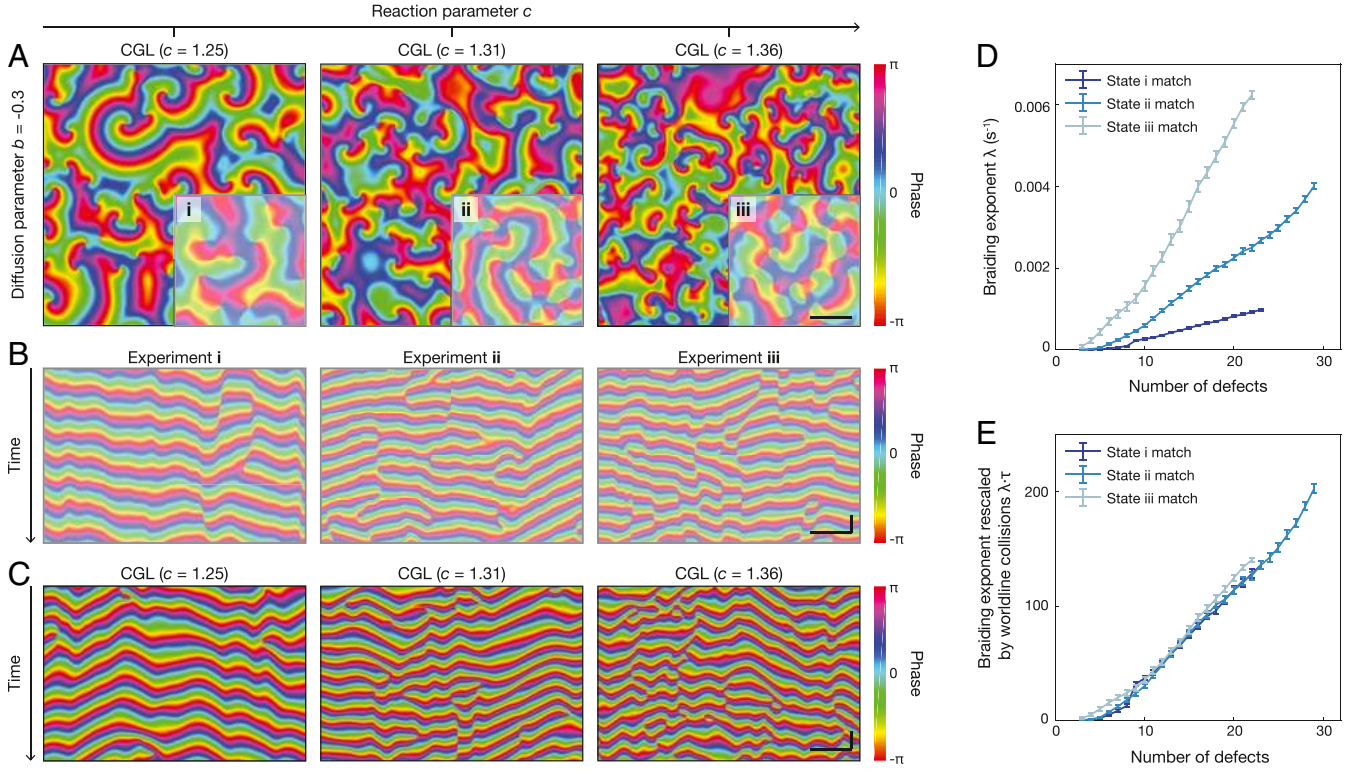

Fig. 4. A generic CGL model captures phase continuum and defect-braiding dynamics with tunable activity. (*A*) Representative snapshots comparing phase fields of best-fit (*Materials and Methods*) CGL (49) models with oocyte states i, ii, and iii (*Insets*), animated in Movie S9. (Scale bar: 20 μm.) (*B*) Snapshots of space–time slices (kymographs) for states i, ii, and iii, animated in Movie S9. (Scale bar: 20 μm; 50 s [vertical]). (*C*) Snapshots of space–time slices (kymographs) for CGL matches of states i, ii, and iii, animated in Movie S9. (Scale bar: 20 μm; 50 s [vertical]). (*D*) Braiding exponents as a function of total defect number exhibit a similar sequential rise in magnitude across CGL matches of states i, ii, and iii. Error bars represent SE across bootstrap samples. (*E*) Braiding exponent curves across CGL matches from *D* consistently collapse when rescaled by the world line collision frequencies. Error bars represent SE across bootstrap samples.

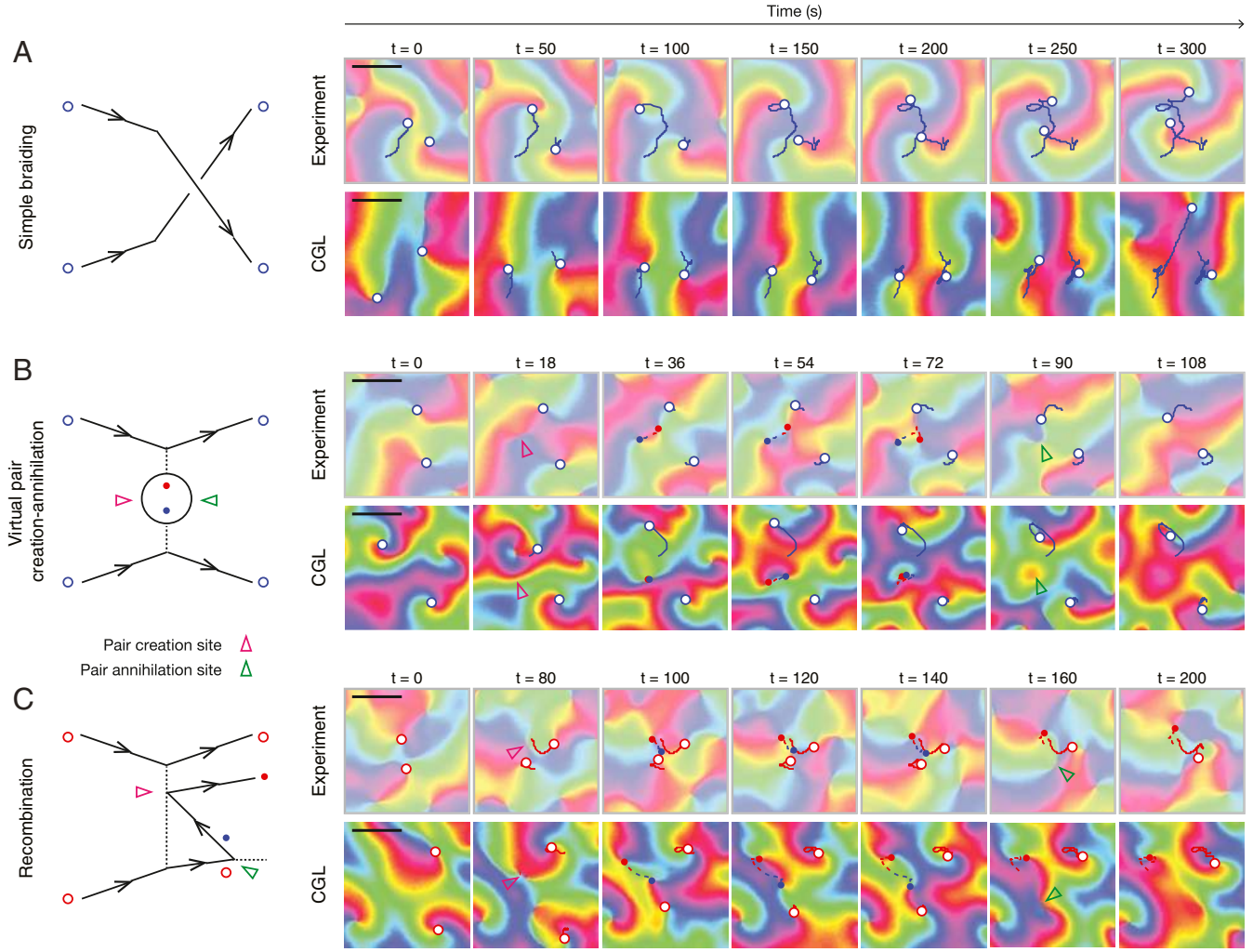

Fig. 5. Pair scattering events observed in experiments and simulations (*Right*), and their corresponding Feynman diagrams (*Left*). (*A*) Scattering event in which a pair of same-sign defects partially braids. From Movie S10: Time-lapse snapshots of an example event in experiment (*Upper*) and the CGL match (*Lower*). (Scale bar: 10 μm.) (*B*) Scattering event between two same-sign defects during which a short-lived "virtual" opposite-sign defect pair is created and annihilated. From Movie S10: Time-lapse snapshots of an example event in experiment (*Upper*) and the CGL match (*Lower*). (Scale bar: 10 μm.) (*C*) Scattering event during which a virtual defect pair is created and recombines with one of the incoming defects. From Movie S10: Time-lapse snapshots of an example event in experiment (*Upper*) and the CGL match (*Lower*). (Scale bar: 10 μm.)

during a 180° braiding operation determines the bosonic, fermionic, or anyonic nature of the fundamental excitations (25). Intriguingly, statistics of braiding defect pairs collected from the CGL states suggest a bosonic exchange symmetry (*SI Appendix*, Fig. S10) associated with the spiral wave system.

Defects as Organizers of Biophysical and Biochemical Signaling. Recent studies of eukaryotic cell layers (19, 28, 35) and bacterial colonies (18) revealed that topological defects play a central role in organizing collective cell dynamics (51), multicellular morphologies (34), and apoptosis (19). Similarly, topological defects at the centers of biochemical (52) and electrical spiral waves (13–16) have been shown to control the collective signaling in multicellular communities, including heart (13–15) and brain tissues (17). Providing an extension to signaling at the single-cell level, our above analysis suggests a link between ATP-driven cellular activity, spiral wave defect dynamics, and information flow on the oocyte membrane (Fig. 2). The eukaryotic Rho-GTP wave patterns studied here bear resemblance to bacterial Min protein oscillations (53), which similarly regulate mechanics during cell divisions (54) and can also realize spiral wave patterns under suitable conditions (55). From a theoretical perspective, the fact that key aspects of the Rho-GTP phase field dynamics can be captured by a generic CGL description (Fig. 4) further supports the hypothesis that topological defect analysis can provide a unifying framework for understanding robust information transport in biological systems. From an experimental perspective, an interesting next challenge is to decipher potential roles of the Rho-GTP membrane signaling defects in the organization of long-wavelength information during mitosis (45). Targeted optogenetic positioning of defects on the cell membrane may help answer this question in the near future.

Conclusions

Groundbreaking research over the last decade has identified topological defects as central organizers of biological information processing and function (17–19). Our analysis of the topological braiding dynamics in biochemical signaling waves on cell membranes demonstrates a framework for comparing information transport and processing in analogy with quantum systems. This paves the way for exploring whether recently developed optogenetic control techniques (23, 24) can enable the creation

and control of emergent bosonic, fermionic, or perhaps even anyonic excitations in biological matter.

Materials and Methods

Additional technical details of experiments and theoretical analysis are described in *SI Appendix*, which includes *SI Appendix*, Figs. S1–S10.

Data Acquisition. For this study, we combined data from previously reported measurements (22) of Rho-GTP steady-state wave patterns on *Patiria miniata* starfish oocyte membranes with data from newly performed experiments (Fig. 2) in which *P. miniata* starfish oocytes were treated with the ATP-depleting drug NaN_3 (sodium azide). In total, the data sets comprise five time series from ref. 22 and four time series from NaN_3 perturbed oocytes (Movie S8). All data were processed using a spectral representation method (*SI Appendix*) that enables previously unfeasible high-resolution phase-field reconstruction and dynamical analysis.

Starfish Oocyte Experiments. Oocytes were extracted from *P. miniata* starfish, washed by calcium-free seawater to prevent spontaneous maturation, and incubated at 15 °C. In vitro–synthesized messenger RNAs were prepared in the laboratory and delivered into cytoplasm via microinjection. Microscope imaging was performed after an overnight incubation to maximize protein expression in oocytes. For each experiment, 1-MA (1-methyl adenine) solution was used to induce meiosis. Fluorescent proteins were excited with a 488-nm laser, focused through a Nikon 60×/NA = 1.40 oil objective and collected using an EMCCD (electron multiplying charge coupling device) camera. The microscope room was maintained at 20 °C to 22 °C throughout the experiment. To obtain the data in Fig. 2, first, the meiosis process was induced until Rho-GTP spiral wave signaling patterns on membrane (time series I) reached a steady state, using the previous protocols (22) for acquiring steady-state data in Fig. 1. Then the oocytes were exposed to the ATP-depleting drug NaN_3 to obtain sequential time-lapse videos II, III, and IV as described in *SI Appendix* and shown in Movie S8.

CGL Simulations. The CGL equation (20),

$$\partial_t \psi = \psi - (1 + ic)|\psi|^2\psi + (1 + ib)\nabla^2\psi,$$

is a generic model describing the spatiotemporal evolution of oscillatory continuum systems $\psi(\mathbf{x}, t)$ near a Hopf bifurcation and can be quantitatively matched to a multispecies reaction–diffusion system (*SI Appendix*). Simulations of the CGL model were performed on a unit sphere using the MATLAB Chebfun library. Each simulation starts from a random initial condition and lasts for sufficient time to ensure decay of initial transient dynamics. A quantitative database and an interactive solver of spatiotemporal patterns of the CGL equation is available online at CGLE Atlas (49).

Data Availability. All data and analyses codes are available in *SI Appendix*. A quantitative database and an interactive solver of spatiotemporal patterns of the CGL equation are available online at CGLE Atlas, https://www.cgleatlas.com/ (49).

ACKNOWLEDGMENTS We thank Melis Tekant and Tzer Han Tan for their help in data acquisition. We thank Cristina Marchetti and Igor Aronson for helpful discussions, and Ned Wingreen for insightful comments. N.F. and J.D. are grateful to the Kavli Institute for Theoretical Physics program "ACTIVE20: Symmetry, Thermodynamics and Topology in Active Matter." This work was supported by a CAREER Award from NSF (N.F.), a Feodor Lynen Fellowship of the Alexander von Humboldt Foundation (J.F.T.), a Complex Systems Scholar Award from the James S. McDonnell Foundation (J.D.), and the Robert E. Collins Distinguished Scholarship Fund (J.D.). This research was supported, in part, by the NSF under Grant NSF PHY-1748958.

1. R. A. Naik, Failure analysis of woven and braided fabric reinforced composites. *J. Compos. Mater.* **29**, 2334–2363 (1995).
2. J.-L. Thiffeault, Measuring topological chaos. *Phys. Rev. Lett.* **94**, 084502 (2005).
3. A. Stern, N. H. Lindner, Topological quantum computation—From basic concepts to first experiments. *Science* **339**, 1179–1184 (2013).
4. H. Rossmanith, M. Doebroenti, M. Albach, D. Exner, Measurement and characterization of high frequency losses in nonideal litz wires. *IEEE Trans. Power Electron.* **26**, 3386–3394 (2011).
5. L. H. Kauffman, S. J. Lomonaco, Braiding, Majorana fermions, Fibonacci particles and topological quantum computing. *Quantum Inform. Process.* **17**, 201 (2018).
6. M. Budišić, J.-L. Thiffeault, Finite-time braiding exponents. *Chaos* **25**, 087407 (2015).
7. T. Bela Bauer *et al*., Topologically protected braiding in a single wire using Floquet Majorana modes. *Phys. Rev. B* **100**, 041102 (2019).
8. U. Tkalec, M. Ravnik, S. Čopar, S. Žumer, I. Muševič, Reconfigurable knots and links in chiral nematic colloids. *Science* **333**, 62–65 (2011).
9. S. Čopar, U. Tkalec, I. Muševič, S. Žumer, Knot theory realizations in nematic colloids. *Proc. Natl. Acad. Sci. U.S.A.* **112**, 1675–1680 (2015).
10. C. Nayak, S. H. Simon, A. Stern, M. Freedman, S. Das Sarma, Non-Abelian anyons and topological quantum computation. *Rev. Mod. Phys.* **80**, 1083–1159 (2008).
11. M. Freedman, A. Kitaev, M. Larsen, Z. Wang, Topological quantum computation. *Bull. Am. Math. Soc.* **40**, 31–38 (2003).
12. J. Lechleiter, S. Girard, E. Peralta, D. Clapham, Spiral calcium wave propagation and annihilation in *Xenopus laevis* oocytes. *Science* **252**, 123–126 (1991).
13. J. M. Davidenko, A. V. Pertsov, R. Salomonsz, W. Baxter, J. Jalife, Stationary and drifting spiral waves of excitation in isolated cardiac muscle. *Nature* **355**, 349–351 (1992).
14. R. A. Gray, A. M. Pertsov, J. Jalife, Spatial and temporal organization during cardiac fibrillation. *Nature* **392**, 75–78 (1998).
15. N. Bursac, F. Aguel, L. Tung, Multiarm spirals in a two-dimensional cardiac substrate. *Proc. Natl. Acad. Sci. U.S.A.* **101**, 15530–15534 (2004).
16. J. Christoph *et al*., Electromechanical vortex filaments during cardiac fibrillation. *Nature* **555**, 667–672 (2018).
17. X. Huang *et al*., Spiral wave dynamics in neocortex. *Neuron* **68**, 978–990 (2010).
18. K. Copenhagen, R. Alert, N. S. Wingreen, J. W. Shaevitz, Topological defects promote layer formation in *Myxococcus xanthus* colonies. *Nat. Phys.* **17**, 1–5 (2021).
19. T. B. Saw *et al*., Topological defects in epithelia govern cell death and extrusion. *Nature* **544**, 212–216 (2017).
20. I. S. Aranson, L. Kramer, The world of the complex Ginzburg-Landau equation. *Rev. Mod. Phys.* **74**, 99–143 (2002).
21. C. Brito, I. S. Aranson, H. Chaté, Vortex glass and vortex liquid in oscillatory media. *Phys. Rev. Lett.* **90**, 068301 (2003).
22. T. H. Tan *et al*., Topological turbulence in the membrane of a living cell. *Nat. Phys.* **16**, 657–662 (2020).
23. R. A. B. Burton *et al*., Optical control of excitation waves in cardiac tissue. *Nat. Photonics* **9**, 813–816 (2015).
24. R. Majumder *et al*., Optogenetics enables real-time spatiotemporal control over spiral wave dynamics in an excitable cardiac system. *eLife* **7**, e41076 (2018).
25. H. Bartolomei *et al*., Fractional statistics in anyon collisions. *Science* **368**, 173–177 (2020).
26. T. Sanchez, D. T. N. Chen, S. J. DeCamp, M. Heymann, Z. Dogic, Spontaneous motion in hierarchically assembled active matter. *Nature* **491**, 431–434 (2012).
27. S. J. DeCamp, G. S. Redner, A. Baskaran, M. F. Hagan, Z. Dogic, Orientational order of motile defects in active nematics. *Nat. Mater.* **14**, 1110–1115 (2015).
28. G. Duclos, C. Erlenkämper, J.-F. Joanny, P. Silberzan, Topological defects in confined populations of spindle-shaped cells. *Nat. Phys.* **13**, 58–62 (2017).
29. L. Giomi, M. J. Bowick, X. Ma, M. C. Marchetti, Defect annihilation and proliferation in active nematics. *Phys. Rev. Lett.* **110**, 228101 (2013).
30. S. Shankar, S. Ramaswamy, M. C. Marchetti, M. J. Bowick, Defect unbinding in active nematics. *Phys. Rev. Lett.* **121**, 108002 (2018).
31. F. Vafa, M. J. Bowick, M. C. Marchetti, B. I.Shraiman, Multi-defect dynamics in active nematics. arXiv [Preprint] (2020). https://arxiv.org/abs/2007.02947 (Accessed 24 May 2021).
32. A. Doostmohammadi, M. F. Adamer, S. P. Thampi, J. M. Yeomans, Stabilization of active matter by flow-vortex lattices and defect ordering. *Nat. Commun.* **7**, 10557 (2016).
33. S. Shankar, M. Cristina Marchetti, Hydrodynamics of active defects: From order to chaos to defect ordering. *Phys. Rev. X* **9**, 041047 (2019).
34. A. Doostmohammadi, S. P. Thampi, J. M. Yeomans, Defect-mediated morphologies in growing cell colonies. *Phys. Rev. Lett.* **117**, 048102 (2016).
35. C. Blanch-Mercader *et al*., Turbulent dynamics of epithelial cell cultures. *Phys. Rev. Lett.* **120**, 208101 (2018).
36. N. Kumar, R. Zhang, J. J. de Pablo, M. L. Gardel, Tunable structure and dynamics of active liquid crystals. *Sci. Adv.* **4**, eaat7779 (2018).
37. A. J. Tan *et al*., Topological chaos in active nematics. *Nat. Phys.* **15**, 1033–1039 (2019).
38. L. Braverman, C. Scheibner, V. Vitelli, Topological defects in non-reciprocal active solids with odd elasticity. arXiv [Preprint] (2021). https://arxiv.org/abs/2011.11543v2 (Accessed 24 May 2021).
39. M. C. Wigbers *et al*., A hierarchy of protein patterns robustly decodes cell shape information. *Nat. Phys.* **17**, 578–584 (2021).
40. A. U. Oza, J. Dunkel, Antipolar ordering of topological defects in active liquid crystals. *New J. Phys.* **18**, 093006 (2016).
41. J. Binysh, Ž. Kos, S. Čopar, M. Ravnik, G. P. Alexander, Three-dimensional active defect loops. *Phys. Rev. Lett.* **124**, 088001 (2020).
42. A. Piekny, M. Werner, M. Glotzer, Cytokinesis: Welcome to the Rho zone. *Trends Cell Biol.* **15**, 651–658 (2005).

43. Y. Fukata, M. Amano, K. Kaibuchi, K. Kaibuchi, Rho-Rho-kinase pathway in smooth muscle contraction and cytoskeletal reorganization of non-muscle cells. *Trends Pharmacol. Sci.* **22**, 32–39 (2001).
44. S. Etienne-Manneville, A. Hall, Rho GTPases in cell biology. *Nature* **420**, 629–635 (2002).
45. W. M. Bement *et al*., Activator-inhibitor coupling between Rho signalling and actin assembly makes the cell cortex an excitable medium. *Nat. Cell Biol.* **17**, 1471–1483 (2015).
46. C. N. Weiler *et al*., Spontaneous vortices in the formation of Bose–Einstein condensates. *Nature* **455**, 948–951 (2008).
47. T. Mawson, T. C. Petersen, J. K. Slingerland, T. P. Simula, Braiding and fusion of non-Abelian vortex anyons. *Phys. Rev. Lett.* **123**, 140404 (2019).
48. C. A. Abad, Introduction to representations of braid groups. *Rev. Colomb. de Mat.* **49**, 1–38 (2015).
49. J. F. Totz, CGLE Atlas. https://www.cgleatlas.com/ (Accessed 28 January 2021).
50. M. E. Peskin, *An Introduction to Quantum Field Theory* (CRC, Boca Raton, FL, 2018).
51. K. Kawaguchi, R. Kageyama, M. Sano, Topological defects control collective dynamics in neural progenitor cell cultures. *Nature* **545**, 327–331 (2017).
52. S. Sawai, P. A. Thomason, E. C. Cox, An autoregulatory circuit for long-range self-organization in *Dictyostelium* cell populations. *Nature* **433**, 323–326 (2005).
53. K. C. Huang, Y. Meir, N. S. Wingreen, Dynamic structures in *Escherichia coli*: Spontaneous formation of MinE rings and MinD polar zones. *Proc. Natl. Acad. Sci. U.S.A.* **100**, 12724–12728 (2003).
54. X. Yang *et al*., GTPase activity-coupled treadmilling of the bacterial tubulin FtsZ organizes septal cell wall synthesis. *Science* **355**, 744–747 (2017).
55. L. Wettmann, K. Kruse, The Min-protein oscillations in *Escherichia coli*: An example of self-organized cellular protein waves. *Phil. Trans. R. Soc. B* **373**, 20170111 (2018).

PNAS
www.pnas.org

Supplementary Information for

Topological braiding and virtual particles on the cell membrane

Jinghui Liu, Jan F. Totz, Pearson W. Miller, Alasdair D. Hastewell, Yu-Chen Chao, Jörn Dunkel and Nikta Fakhri

Nikta Fakhri, Jörn Dunkel.
E-mail: fakhri@mit.edu, dunkel@mit.edu

This PDF file includes:

Other supplementary materials for this manuscript include the following:

Supporting Information Text

Materials and Methods

Membrane signaling wave dataset from live starfish oocytes. To obtain high-resolution Rho-GTP intensity and defect trajectory data, we developed and implemented a spectral representation framework, which is described in detail in the next Section and Fig. S2. We applied this framework to five videos showing steady-state Rho-GTP wave patterns at different levels of cellular activity (Fig. 1B; Movie S2-6, left panel) and four sequential videos of Rho-GTP wave patterns with cellular activity perturbed by ATP depletion treatment. The five steady-state videos were recorded as part of our previous study (1). All raw microscope image data were de-noised and interpolated using a spectral representation approach, which by projecting the measured pixelated fields onto spatiotemporal basis functions allows for a systematic data de-noising and compression and translated discrete video data into continuous differentiable fields that can be computed at arbitrary spatiotemporal resolution. We then used this representation to generate de-noised evaluations of raw microscope data at 2 times higher spatial resolution and 10 times higher temporal resolution for dynamical analyses.

The experimental recordings of the five steady-state signaling wave data were obtained as described in our previous study (1), by preparing the starfish oocytes with the following procedures. *Patiria miniata* starfish were procured from South Coast Bio-Marine LLC, then kept in a salt-water fish tank maintained at 15°C. Ovaries from the female animals were extracted through a small bottom incision (animals heal after extraction) made near the central disk. Upon extraction, ovaries were carefully fragmented with a pair of scissors to release the oocytes. The oocytes were then washed twice with calcium-free salt-water to prevent early initiation of meiosis. The washed oocytes were incubated in regular salt-water at 15°C for up to three days, within which experiments were performed.

Two types of proteins were co-expressed in the oocytes prior to measuring membrane Rho-GTP signaling waves. To fluorescently label Rho-GTP molecules, we used the eGFP-rGBD (fluorescently-labelled rhotekin binding domain) construct, a gift from William Bement (2) (Addgene plasmid 26732; http://n2t.net/addgene:26732; RRID: Addgene 26732.). To generate excitable Rho-GTP waves on the membrane, we used the Ect2-T808A-mCherry construct, which was a kind gift from G. von Dassow. Ect2 (epithelial cell transforming sequence 2) is a conserved guanine exchange factor (GEF) enzyme involved in Rho protein activation in starfish oocyte (3–5) as well as broader types of animal cells (6). The Ect2-T808A molecule bears a mutation that desensitizes it to one particular Cdk1 phosphorylation in starfish oocytes, which otherwise limits membrane association during the M-phase. Both constructs were amplified with overnight bacterial culturing, purified (Miniprep kit, Qiagen) and linearized (with appropriate restriction enzymes), and eventually used as templates to synthesize mRNA (SP6 mMessage mMachine transcription kits, Thermo Fisher Scientific). The synthesized mRNA molecules were mixed in nuclease-free water solution, then microinjected into the cytoplasm of the oocytes. Injected oocytes were incubated overnight at 15°C to allow for sufficient protein expression.

To image the membrane Rho-GTP signaling waves with minimized positional drifts, we used a set of specially-designed PDMS (polydimethylsiloxane) chambers for containing the oocytes (5) (Fig. S1A). The chambers were microfabricated by casting gas-permeable PDMS onto patterned silicon wafer moulds. We designed the elliptical shape of the master mould to match typical volumes of the oocytes, with a height of 80 µm and surface area of $\sim 27\,000\,\mu m^2$. The patterned silicon wafer was manufactured using photolithography (Microfactory SAS), and silicon wafer was silanized with trichlorosilane (Sigma 448931). To prepare the chambers, PDMS was first made by mixing Dow SYLGARD 184 Silicone Elastomer Clear solution at a 10:1 base-to-curing agent ratio. After mixing thoroughly, the elastomer was poured over the silicon master mould, then degassed in a vacuum chamber and cured at $60\,^{\circ}C$ in an oven for an hour.

The imaging of membrane Rho-GTP signaling waves of the five-oocyte dataset was performed using a Zeiss 700 laser scanning confocal system, which contains a Zeiss AxioObserver motorized inverted microscope stand and three photomutiplier detectors. To induce meiosis, we first treated microinjected oocytes with 10 µM 1-methyl adenine solution (Sigma 215325). The treated oocytes were then washed with regular salt-water and loaded into PDMS chambers (Fig. S1A). Time-lapse confocal images collecting near-membrane Z-stack signals (Fig. S1B) were acquired using a ×40/NA 1.3 oil Plan Apochromat objective with appropriate laser lines and emission filters. The steady-state wave dataset (Movie S2-S6) was collected from five individual oocytes in two different batches. Movie S1 showing the representative time evolution of Rho-GTP patterns was acquired using a RPI spinning disk confocal microscope with a ×40/NA 1.3 oil Plan Apochromat objective and oocyte was collected from a separate batch, but all other treatments are conserved. During imaging, the microscope room was always maintained at 20 - 22°C.

To obtain the four sequential time-lapse videos of Rho-GTP wave pattern data under ATP depletion, we applied the mitochondrial inhibitor drug sodium azide NaN_3 (Sigma 71289) to individual starfish oocytes during their steady-state Rho-GTP signaling process. After the induction of meiosis, protein-expressing oocytes were transferred to an open chamber constructed from a glass coverslip and a gas-permeable polymer coverslip (ibidi sticky-Slides) spaced by two parallel lanes of $100\,\mu m$-thick double-sided Scotch tapes. Throughout imaging, we immersed the chamber in a $400\,\mu L$ filtered seawater droplet to prevent evaporation. The chamber has two open ends, therefore permitting perturbation of oocyte metabolism through application of inhibition drug into the open seawater droplet.

For ATP depletion experiments, we added sodium azide to the open droplet after the oocytes exhibited membrane Rho-GTP waves with steady spatial and temporal structures. The imaging of Rho-GTP waves in open-chamber cells was performed using a home-built optical setup with 488 nm laser (50 mW, OBIS, Coherent Inc.) excitation. A neutral-density filter (NDC-50C-4M, Thorlabs) was used to adjust the intensity of the 488 nm laser beam. The beam diameter was expanded using two lenses with focal lengths $f_1 = 40$ mm and $f_2 = 300$ mm (Thorlabs). The

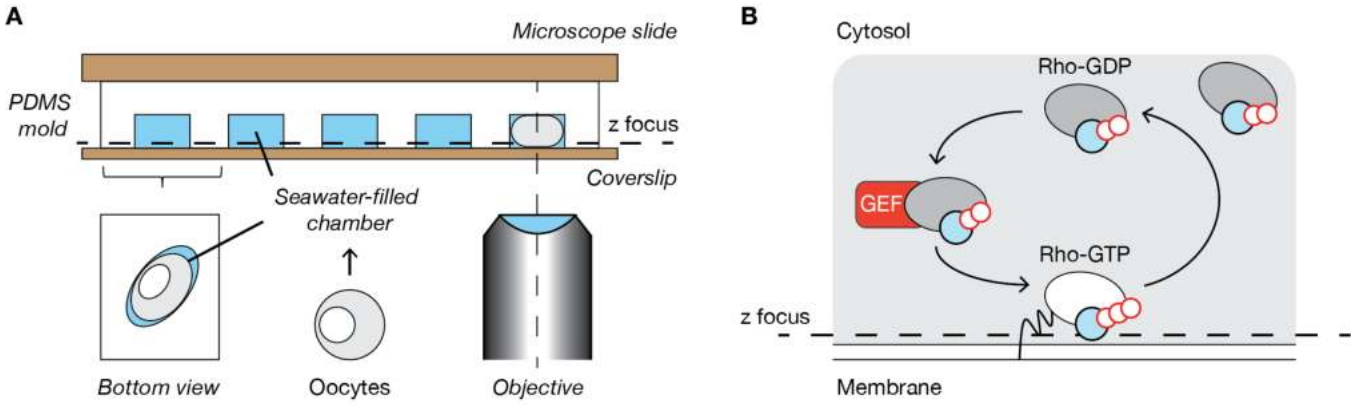

Fig. S1. Experimental setup and Rho protein reaction kinetics. (A) Experimental setup to visualize membrane fluorescence accompanying Rho protein signaling waves. Oocytes were confined in seawater-filled PDMS chambers during time-lapse imaging. (B) Cycling of Rho protein between the GTP-bound form (active, fluorescently labelled in experiments) on the membrane and GDP-bound form (inactive) in the cytosol. GEF (guanine nucleotide exchange factor) enzyme catalyzes the activation process. Confocal images were collected from near-membrane Z-stack signals.

expanded beam was circularly polarized using a quarter-wave plate (WPQ05M-561, Thorlabs) and then focused into the back aperture of a high-NA (numerical aperture) oil objective (Nikon CFI Plan Apo 60X/NA=1.40). Emitted fluorescent light was collected through the same objective, passed through a custom made dichroic beam splitter (ZT405/488/561/700-800, Chroma), filtered using a single band-pass filter (FF01-531/46-25, Semrock), and eventually focused onto a EMCCD camera (Andor, Oxford Instrument). Time-lapse images were focused on a single near-membrane z-position and taken at 2 frames per second. We collected four consecutive time series for the oocyte shown in Fig. 2 and Movie S8 (time series I, II, III and IV), each of 30 min duration, with <3 min intervals in between to start drug treatment (in between time series I and II) or adjust z-focus ((in between time series II, III and IV)).

Data representation, phase field construction and phase defect tracking from signaling waves. We constructed the phase field from microscope images with the following procedure. Raw time-lapse Z-stack images (covering ∼5 µm near the membrane) were first combined into a single intensity field video through a maximal intensity projection. The rectangular intensity field video, $I(\mathbf{x}, t)$, was extracted from the experimental intensity video by least square fitting an ellipse to the boundary of the oocyte. The data was then rotated to axis align the major and minor axes of the ellipse. The rectangular region was extracted by choosing the largest possible rectangle inscribed in the ellipse. Similar to spectral methods for differential equations, the (2 + 1)D space time data cube with N_x, N_y and N_t pixels in each dimension respectively is represented as a sum over bases functions, Chebyshev polynomials of the first kind in space and Fourier in time (7),

$$I(\mathbf{x}, t) = \sum_{n=0}^{N_x-1} \sum_{m=0}^{N_y-1} \sum_{k=-N_t/2}^{N_t/2-1} c_{n,m,k} T_n(x) T_m(y) e^{2\pi i k t/N_t}. \quad [1]$$

$T_n(x)$ is the n degree Chebyshev polynomial of the first kind, $T_n(x) = \cos(n \arccos(x))$. Assuming the data $I(\mathbf{x}, t)$ can be well represented by a smooth function $f(x, y, t)$ with additive noise, $I(\mathbf{x}, t) = f(x, y, t) + \epsilon_{x,y,t}$ where $|\epsilon| \ll |f|$, then the linearity of the Fourier and Chebyshev transform implies the coefficients $c_{n,m,k}$ can be decomposed as the sum $c_{n,m,k} = \tilde{c}_{n,m,k} + \tilde{\epsilon}_{n,m,k}$, where the $\tilde{c}_{n,m,k}$ decay rapidly because they come from a smooth function and the $\epsilon_{n,m,k}$ are uniformly small relative to the largest $\tilde{c}$. We therefore expect that we can remove noise and get a smooth representation of the data by cutting off the summation in Eq. (1) at the thresholds M_c and M_f to get the new denoised representation of the data,

$$f(\mathbf{x}, t) \approx \sum_{n,m=0}^{(Ny/Nx)n+m \le M_c} \sum_{k=-M_f}^{M_f} c_{n,m,k} T_n(x) T_m(y) e^{2\pi i k t/N_t}. \quad [2]$$

The coefficients $c_{n,m,k}$ can be calculated efficiently using fast algorithms for the Discrete Cosine Transform and the Discrete Fourier Transform (8, 9). This assumes that the function is sampled on the Chebyshev grid $x_k = \cos(k\pi/N)$ for $k = 0, \ldots, N$ in both spatial dimensions and uniformly spaced in time. The data is converted from the uniformly spaced experimental grid to the Chebyshev grid using linear interpolations. The errors introduced in the coefficients from the linear interpolations are of lower order than the error already introduced from the noise in the data.

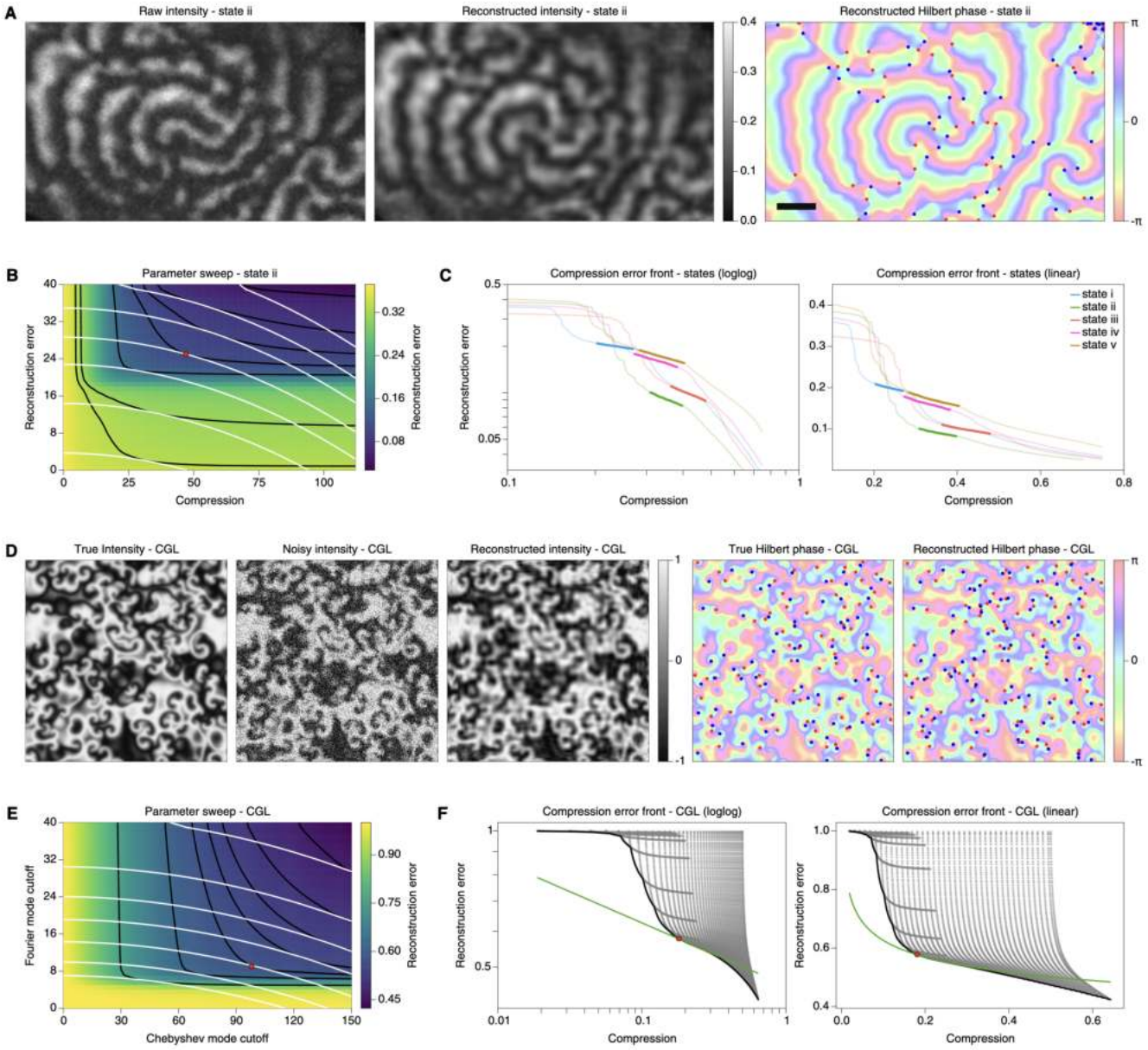

Fig. S2. Data representation and reconstruction using orthogonal basis projection. (A) Comparison of an experimental snapshot with the corresponding data and phase field representation Eq. (2) for state ii. Scale bar 20 μm. (B) Parameter sweep over possible Fourier and Chebyshev mode cutoffs for state ii. (C) Compression error fronts for the experimental states. We see that all the curves have a similar shape across all states. The linear fit to each of the experimental fronts on the loglog graph is shown with thick lines. (D) Comparison of true and represented data and phase for simulated CGL test data. (E) Parameter sweep over possible Fourier and Chebyshev mode cutoffs for the CGL test data. (F) Compression error front extracted from the parameter sweep in (F) along with the linear fit to the loglog curve and the chosen cutoff point.

The thresholds M_c and M_f are chosen by sweeping over all possible thresholds $0 \leq M_c \leq N_y$ and $1 \leq M_f \leq N_t/2$ and calculating the relative reconstruction error,

$$\mathcal{E}(\rho, \tilde{\rho}) = \frac{\sqrt{\sum_{\mathrm{x},t}(I(\mathbf{x},t) - f(\mathbf{x},t))^2}}{\sqrt{\sum_{\mathbf{x},t} I(\mathbf{x},t)^2}} \qquad [3]$$

and the effective compression at each point. The effective compression is defined by the mean of the spatial and temporal compression $C = 0.5(C_s + C_t)$ where $C_t = (2M_f + 1)/(2N_t + 1)$ and $C_s = (2 + 2M_c - N_y)(1 + N_x)/(2N_xN_y)$. A scatter plot of compression versus reconstruction error shows that there is a front corresponding the points of best reconstruction error for a given compression. These correspond to points where the reconstruction error contours and compression contours are tangent. We choose the threshold as the point at the start of the elbow of this front determined by fitting a line to the linear part of the curve on a loglog plot. Once we have the basis representation for the experimental data we can then evaluate the expansion in Eq. (2) at any points (x, y, t) inside the domain interpolating the data at higher

resolution.

The method was first tested on mock CGL data with added Poisson noise of varying strengths to approximate experimental noise. Fig. S2E-F illustrates the process for choosing the thresholds and S2D show a comparison of the resulting reconstruction to the noisy input image and the true image for one noise strength. For the experimental data, parameter sweeps were performed for each state and a cutoff was chosen for each state (Fig. S2A-C). For the ATP depletion data an initial preprocessing step was used to account for the background in the raw microscope image. Each frame was first down sampled by averaging over each square of four neighboring pixels and then rescaled to have zero mean and standard deviation of one. The mean over all rescaled frames was then subtracted from each frame to remove the background illumination. Since the resolution is the same across all ATP depletion videos, the same cutoff was used, which was chosen by selecting the largest Chebyshev and Fourier threshold across all the parameter sweeps from each video. The denoised expansion was then evaluated at 2 times higher spatial resolution and at 1 frame per second temporal resolution. (Raw videos have frame rates of 10 –12 s and pixel resolution of $0.625\,\mu\text{m}$.)

The stationarity of all Rho-GTP wave data used for further statistical analysis was ensured by selecting from experimental videos the time series with quasi-constant pixel oscillation period, spatial wavelength and defect density, same as the protocol used in (1). This test was performed for all five steady-state data as well as the initial time series (I) of the ATP-depleted dataset, to ensure that patterns were at steady state before exposure to drug treatment in sequential time series (II, III and IV).

The phase was calculated from the new data representation. Let τ be the approximately a quarter of the oscillation period of the oscillating time signal of each pixel. First the moving center, $\bar{I}(t)$, calculated by convolving the signal with a gaussian window of width τ, was subtracted from each pixel. This centers the pixel time signal around 0. Next we computed the analytic extension of each pixel trajectory $(I-\bar{I})(t)$ into the complex plane, $z(t) = (I-\bar{I})(t) + \text{HT}[(I-\bar{I})(t)]$, where $\text{HT}[(I-\bar{I})(t)]$ is the Hilbert transform of the signal (10). In the frequency domain this corresponds to setting all coefficients corresponding to negative frequencies to 0 and doubling those corresponding to positive frequencies. For a discrete signal of length N with discrete Fourier coefficients $\hat{I}_k$ this corresponds to,

$$\hat{z}_k = \begin{cases} 2\hat{I}_k & \text{for } 1 \le k \le \frac{N}{2} - 1 \\ 0 & \text{for } \frac{N}{2} + 1 \le k \le N-1 \\ \hat{I}_k & \text{for } k = 0 \text{ or } k = \frac{N}{2} \end{cases}. \qquad [4]$$

We then define the phase of the signal $\phi(t)$ as the angle of the analytic signal in the complex plane $\phi(t) = \tan^{-1}(\text{HT}[(I-\bar{I})(t)], (I-\bar{I})(t))$. The extraction was performed for every individual pixel in the microscope images to obtain the time-lapse phase field, $\phi(\mathbf{x}, t)$.

The phase defects were subsequently tracked based on the reconstructed phase field. To locate the positions of phase defects harbored in the phase field of an instantaneous time frame, $\phi(x)$, we performed a line integral $\oint_C \nabla\phi(\mathbf{x}) \cdot d\mathbf{s}$ for every two-pixel-by-two-pixel local window. Plus (minus) phase defects have a value of 2π (-2π). To retrieve the trajectories of phase defects through continuous time frames, we used a particle-tracking software with a gap-closing algorithm (developed by J.-Y. Tinevez). This software is based on the Munkres/Hungarian algorithm and is available from the FileExchange site on the MathWorks website (https://www.mathworks.com/matlabcentral/fileexchange/34040-simpletracker).

Extracting loops and loop statistics from phase defect trajectories. To obtain loops from phase defect trajectories, we first identified defect creation and annihilation sites at each time frame. A leading distance cutoff d = 16 pixels ($\sim 10\,\mu\text{m}$) was used to identify if a pair of oppositely-charged defects that appears (disappears) on the same time frame came from (into) the same creation (annihilation) event. A next correction was implemented for the "breaks" of phase defect trajectories in space-time, where the defects were far from the spatial boundary but appeared (disappeared) without a creation (annihilation) partner. These trajectory breaks originate dominantly from the occasionally high instantaneous defect speeds. The correction was done by allowing for a larger distance cutoff, $d^{'}$ = 40 pixels, to match between breaks within one instantaneous time frame (unidentified creation or annihilation events) as well as between consecutive time frames (unidentified gap in tracking). The latter correction was also incorporated to optimizing performance of the gap-closing tracking algorithm of phase defects. Values of d and $d^{'}$ were empirically determined by their performance of creating and correcting defect trajectory breaks in the experimental dataset.

We next extracted loops from the defect trajectories and creation (annihilation) information. A loop is identified to be the space-time trajectory group connected by multiple creation and annihilation events, where for every single trajectory there is a creation partner and an annihilation partner inside the group. Short-lived loops that only existed for one time frame (and therefore only contain one short-lived plus and minus defect pair) were filtered.

The prominence of defect loops in space-time for experimental wave states strongly correlates with their virtual particle pair creation and annihilation frequencies, resulting in the noticeable difference between state i and v in three-dimensional space-time view (Fig. S3A). To quantify a proper loop metric in three-dimensional space-time, we took the loop arc length, which combines the projection in positional space as well as on time axis (Fig. S3B). The arc length is normalized by the corresponding spatial and temporal periods (Table S1) and is therefore a dimensionless number. The statistics of normalized loop arc lengths across experimental wave states is presented in Fig. S3C). This dimensionless loop metric falls on similar ranges across varying states (Fig. S3D). Fitting the distribution with an exponential function, the

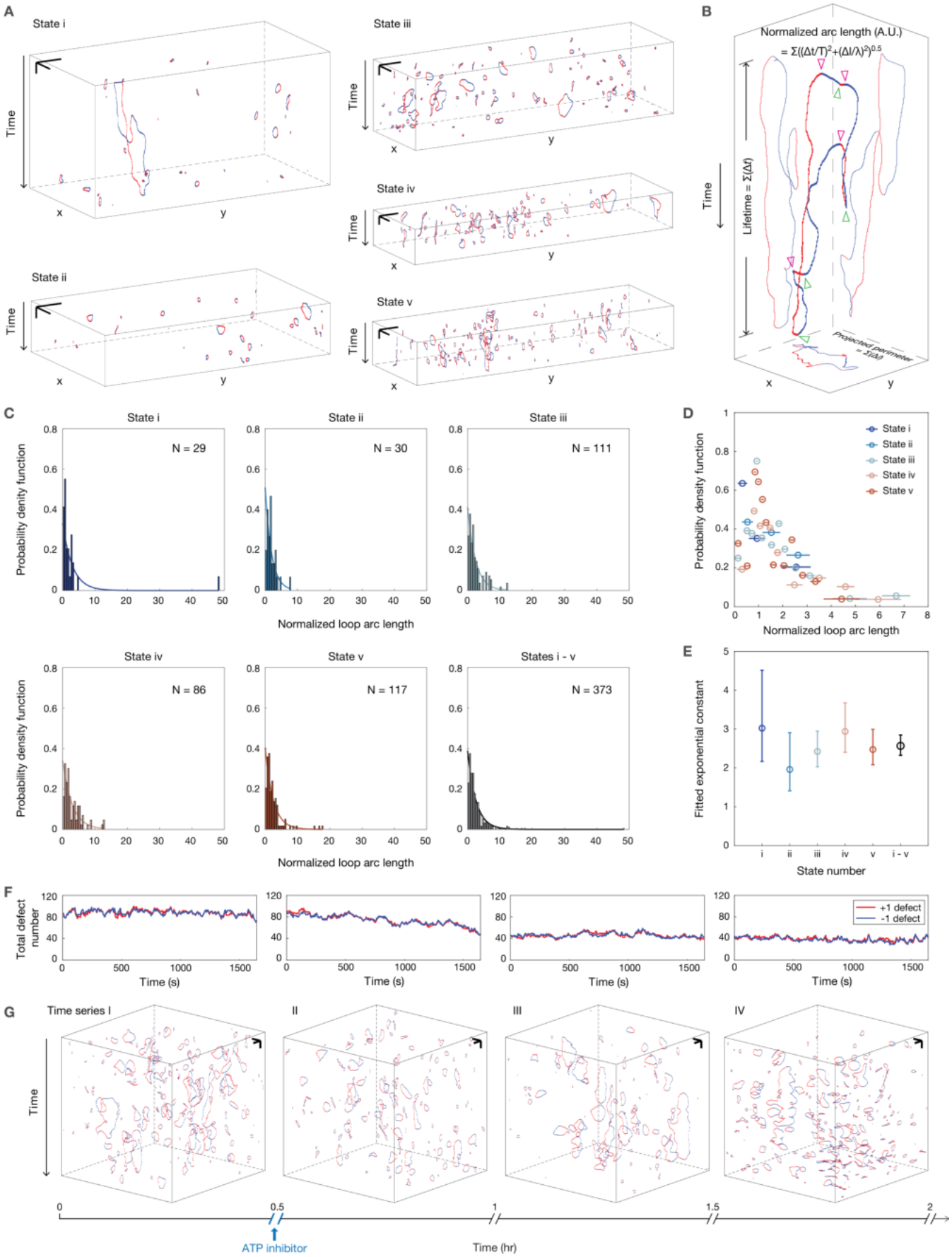

Fig. S3. *(next page)* **Appearance and statistics of space-time defect loops in experimental wave patterns.**

Fig. S3. *(preceding page)* **Appearance and statistics of space-time defect loops in experimental wave patterns.** (A) Space-time view of defect loops formed from defect +1/-1 pair creation and annihilation events in steady-state experimental wave states i - v. Scale bar: $20\,\mu\mathrm{m}$; $120\,\mathrm{s}$ (vertical). (B) Normalized loop arc length as a dimensionless loop metric is calculated from combining loop projections in positional space (projected perimeter, $\Sigma\Delta l$) and on time axis (lifetime, $\Sigma\Delta t$), respectively normalized by the spatial wavelengths λ and temporal oscillation periods T, which we extract from the wave patterns (Table S1). (C) Histograms of the normalized loop arc length for state i – v each as well as i - v's combined statistics. Solid lines show the corresponding exponential fits. (D) Probability density function of normalized loop arc lengths for state i - v. Error bars represent the standard deviation within each equi-probable bin (N = 9 per bin). (E) Scale parameter μ's estimates according to an exponential distribution $p(x) = \frac{1}{\mu}e^{-\frac{x}{\mu}}$ for the normalized loop arc length distributions fall in close values for state i - v and their combined statistics. Error bars represent the 95% confidence intervals of the parameter estimates. (F) Total defect number as a function of time measured in wave patterns before and after ATP depletion. Left to right: Drug-perturbed wave pattern time series I - IV. (G) Space-time view of defect loops in drug-perturbed wave pattern time series I - IV. Scale bar: $20\,\mu\mathrm{m}$; $120\,\mathrm{s}$ (vertical).

maximal-likelihood estimates of the scale parameter also return similar values (Fig. S3E). In the experiments where we perturbed cellular activity with ATP depletion, we see a quantitative change in the density and appearance of space-time defect loops correlating with the shift in defect density (Fig. S3F-G).

Quantifying braiding dynamics from phase defect trajectories. As a topological measure of complexity in dynamical systems, braiding analysis has the advantage that it is well grounded in group theory. Mathematically, a sequence of braiding history between particles can be treated as a series of sequentially multiplied generators, where each generator denotes the direction of "crossing" between one particle and its neighbors projected onto a reference line at an instantaneous time. Analyzing such product of generators as a function of time then gives a measurement of complexity growth in the system.

To quantify the braiding dynamics, we implemented the reduced Burau representation of the n-particle braid group, setting the integer coefficient as $t = -1$ (11). With this representation, each generator $\sigma^{(j)} \in \sigma_i, \sigma_i^{-1}$ becomes an $(n-1) \times (n-1)$ matrix, multiplying one another in the total running matrix product:

$$\Sigma^n(t) = \sigma^{(N)}\sigma^{(N-1)} \cdots \sigma^{(1)} \quad [5]$$

Where N is the total number of crossing events during time t. The matrix product $\Sigma^n(t)$, as a function of time, can be numerically calculated from detecting crossings in particle trajectories, since the generators have well-defined mathematical forms:

$$[\sigma_i]_{kl} = \delta_{kl} + \delta_{k,i-1}\delta_{li} - \delta_{k,i+1}\delta_{li} \quad [6]$$

$$[\sigma_i^{-1}]_{kl} = \delta_{kl} - \delta_{k,i-1}\delta_{li} + \delta_{k,i+1}\delta_{li} \quad [7]$$

($i = 1, \cdots, n-1$ is the positioning of crossing particles on the reference line; $k, l = 1, \cdots, n-1$ are the subscripts of the $(n-1) \times (n-1)$ matrix elements.)

The matrix product $\Sigma^n(t)$ records the braiding history of particles and therefore contains information about the system dynamics. One important piece of information is the magnitude of its largest eigenvalue, $E^n(t)$, often termed as the braiding factor. In random matrix theory, the exponential growth rate of $E^n(t)$ at long time limit approximates the Lyapunov exponent of a chaotic system, which has also been verified in numerical experiments (12). Such exponential growth rate is therefore termed as the braiding exponent,

$$\lambda(n) = \lim_{t\to\infty} \frac{1}{t} \cdot \ln \mid E^n(t) \mid \quad [8]$$

For our two-dimensional defect trajectories, the braiding factor calculated from taking the average of all reference line projections (12) (spanning $[0, \pi]$ with an increment of 0.01π) displayed consistently positive braiding exponents $\lambda(n)$.

Ideally, the matrix product $\Sigma^n(t)$ and the braiding exponent $\lambda(n)$ can be calculated from any number of particles (n) with long enough time frames (t). However, when adopting such analysis for phase defect trajectories, apparently the number of co-existing long-lived phase defects scales inversely with the number of time frames we set. We therefore implemented the following strategy adapted from similar previous finite-trajectory braiding analyses (12): For each wave state, a maximal rectangular observation window was first chosen from regions excluding the low-defect-density area, to ensure that sampled defects are fair tracer particles organizing the wave patterns (Fig. S4A). A library in equal amount of longest-living plus and minus defects were then set up (Fig. S4B), $n_+ = n_- = n_l/2$, where n_l is the upper limit of when the matrix product $\Sigma^n(t)$ can still give a quantifiable braiding exponent $\lambda(n)$ (Fig. S4C-D). The braiding exponent curves were then constructed as a function of defect amount by bootstrapping samples containing varying numbers of defect trajectories from this pre-built braiding library.

We took the following precautions during defect bootstrapping, as braiding is a topological measurement built from projected path-crossing. Each bootstrap sample was taken from defects clustered in neighboring regions (Fig. S5A). For each bootstrap sample we took at defect number n, we quantified the braiding factor growths during the longest shared-trajectory times (Fig. S5B), and averaged over all bootstrap samples to retrieve the braiding exponent corresponding to defect number n. Technically, the braiding factor growth is also affected by the total area that the same number of defect trajectories could occupy differently (Fig. S5C), as well as the unevenness in their spatial distribution. To minimize such effect in the braiding exponent curve, we calculated the total available sample amount n_{bs} at each defect number n, and required that $n_{bs} > 50$ for the braiding exponent to be included in the curve in Fig. 3C. Also, we excluded the defect number n at which the growth of trajectory-occupied-area deviates a linear growth (Fig. S5D). Both metrics similarly omit the braiding exponent curves at defect numbers n

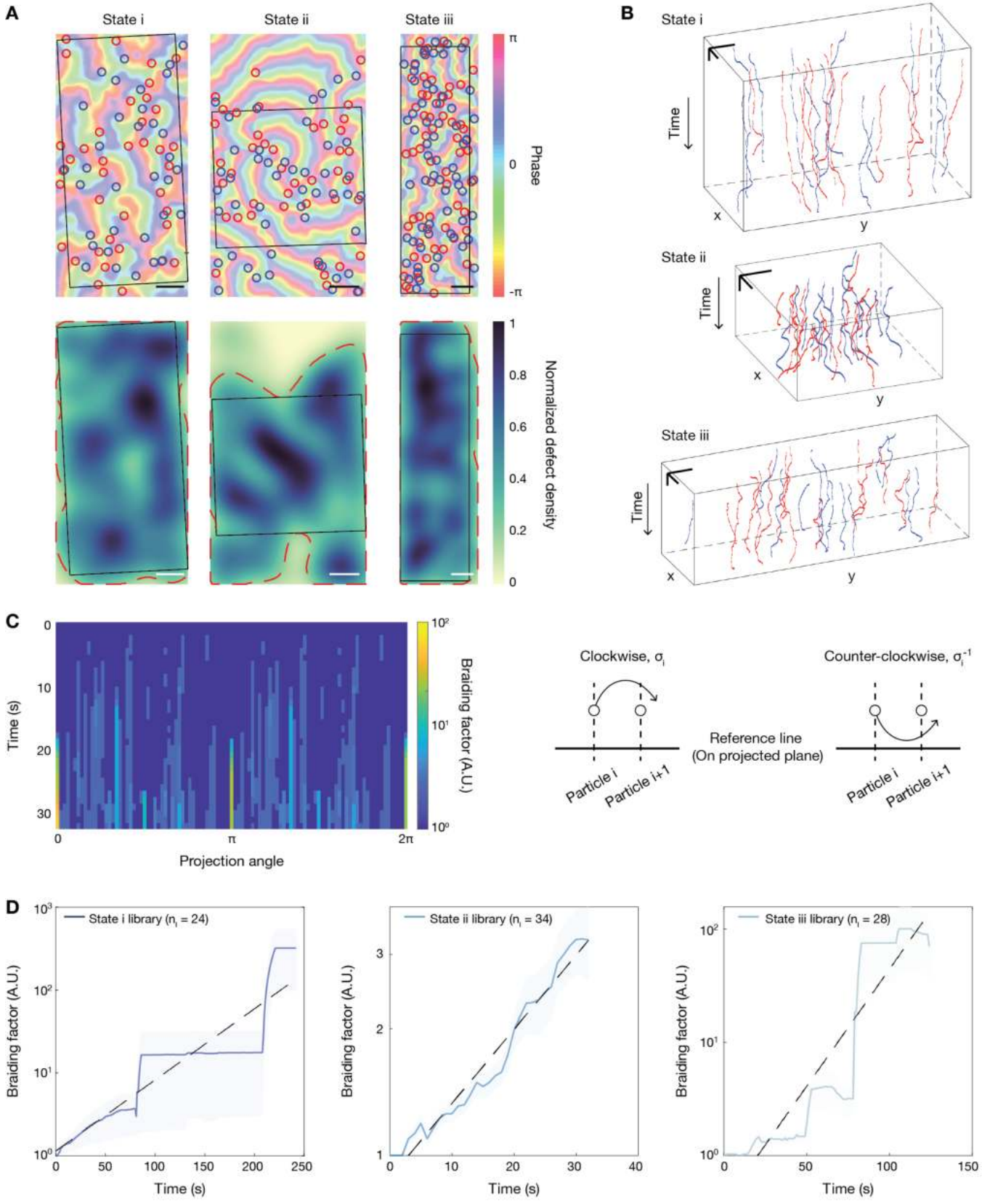

Fig. S4. *(next page)* **Quantifying braiding dynamics of phase defects in experimental wave patterns.**

Fig. S4. *(preceding page)* **Quantifying braiding dynamics of phase defects in experimental wave patterns.** (A) Selection of observation windows for phase defects for experimental state i - iii (top row) based on the normalized defect density distribution in positional space (bottom row). The density heatmap was constructed by applying a two-dimensional Gaussian kernel of standard deviation $10\,\mu\mathrm{m}$ for every presence of phase defect in space and average over time frames. Density cutoff (red dashed line) was set at $\rho_0 = 0.2$. Scale bar: $20\,\mu\mathrm{m}$ (B) Libraries of phase defect trajectories constructed across state i - iii. Scale bar: 20 µm; 120 s (vertical). (C) Left: Heatmap visualizing the braiding factor growth of a collection of particle trajectories across a rotating reference line (projection angle). The phase defect trajectory library of state ii was used to generate this heatmap. Right: Schematic for detecting two alternative particle-particle crossing paths that correspond to different braiding group generators. (D) Braiding factor growths calculated for state i – iii. Curves are quantified from the entire library for each state. Shaded regions represent the standard error across reference line projections.

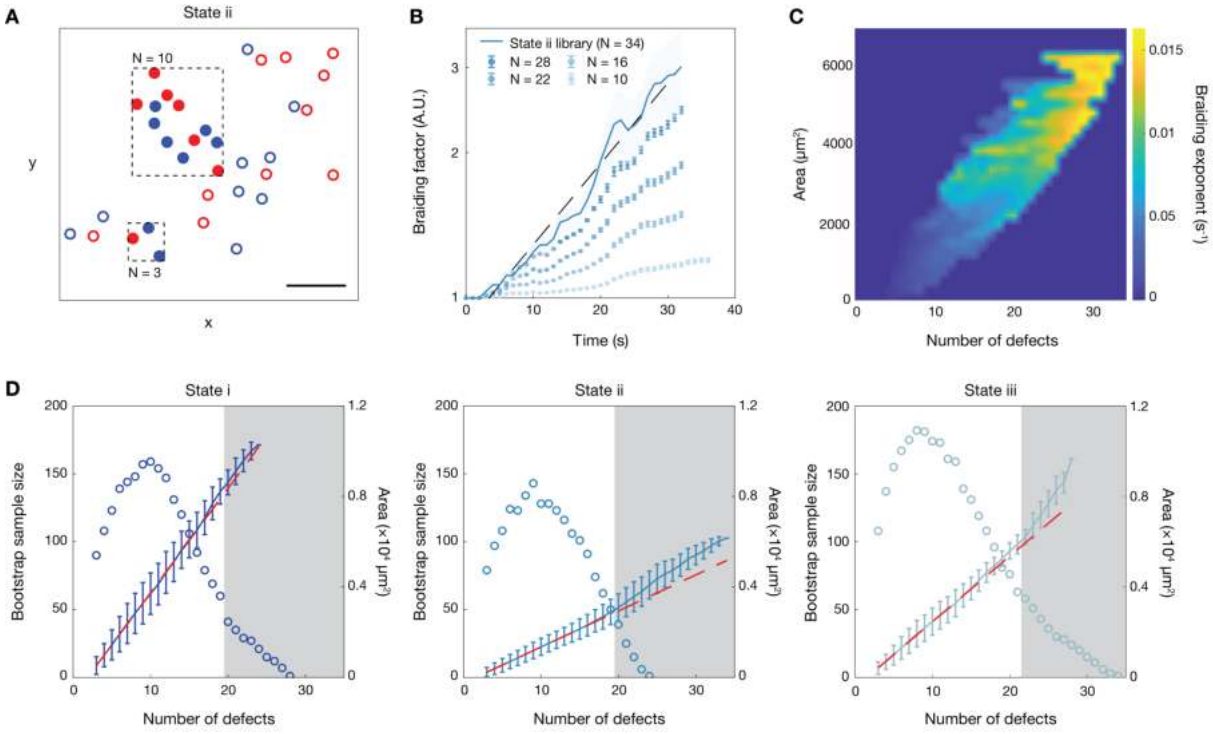

Fig. S5. Construction of braiding exponent curves through bootstrapping phase defect trajectories within a pre-built library. (A) Schematic of neighboring-trajectory-bootstrapping within the phase defect library. Shown here is the mean position of all defects in the library for state ii. Scale bar: 20 µm. (B) Braiding factor growths calculated for state ii. Top curve is quantified from the entire library (N = 34, shaded regions represent the standard error across reference line projections) and lower curves are from the bootstrap samples taken for trajectory number N = 10, 16, 22, 28. Error bars represent the standard error across bootstrap samples. (C) Heatmap visualizing the distribution of braiding exponents evaluated from bootstrap trajectory samples with varying defect number and spatial area coverage. (D) Amount of available bootstrap samples and the mean area each sample cover as a function of number of defects for state i - iii. Error bars represent the standard deviation across samples. Shaded regions in grey are the number-of-defect cutoffs chosen for the braiding exponent curves for each state.

approaching the size of the library n_l (grey region in Fig. S5D). Finally, we were able to extract the mean value of braiding exponent $\lambda(n)$ from bootstrapped samples, and quantify it as a function of defect number, n (Fig. 3C-D).

This bootstrapping strategy has qualitative influences when comparing the braiding curves we extracted from experimental defects and continuum complex Ginzburg-Landau simulations (next section). The data collapse in Fig. 3D deviates at larger defect number, and the reason is as follows: Our experimental setup where oocytes are confined in PDMS chambers provides the flat surface necessary for time-lapse microscopy imaging. Meanwhile, it also generates a finite curvature difference between defects that are located near the boundary when compared to those in the center. Limited by the finite defect amount available in experiments, we included near-boundary defects in our calculations. These boundary defects contribute to the deviation of braiding exponent at large defect numbers, as bootstrapping of trajectories renders the number of sampled trajectory sets fewer for large defect numbers, and contain more of the boundary defects.

Simulating continuum complex Ginzburg-Landau models on a sphere. Simulations for Fig. 4 were performed on the domain of a unit sphere using the Chebfun package, a publicly available PDE solver (13). The methodology used is identical to that previously described in Ref. (1). For completeness, we used a time step of 0.1 for the temporal evolution and 256 spectral modes to resolve the spatial domain.

A quantitative database and an interactive solver of spatiotemporal patterns in the complex Ginzburg-Landau equation can be viewed online at: CGLE Atlas, https://www.cgleatlas.com. The interactive simulation requires the latest version of Firefox/Safari and Javascript as well as a graphics card on the client computer with at least 1 GB RAM.

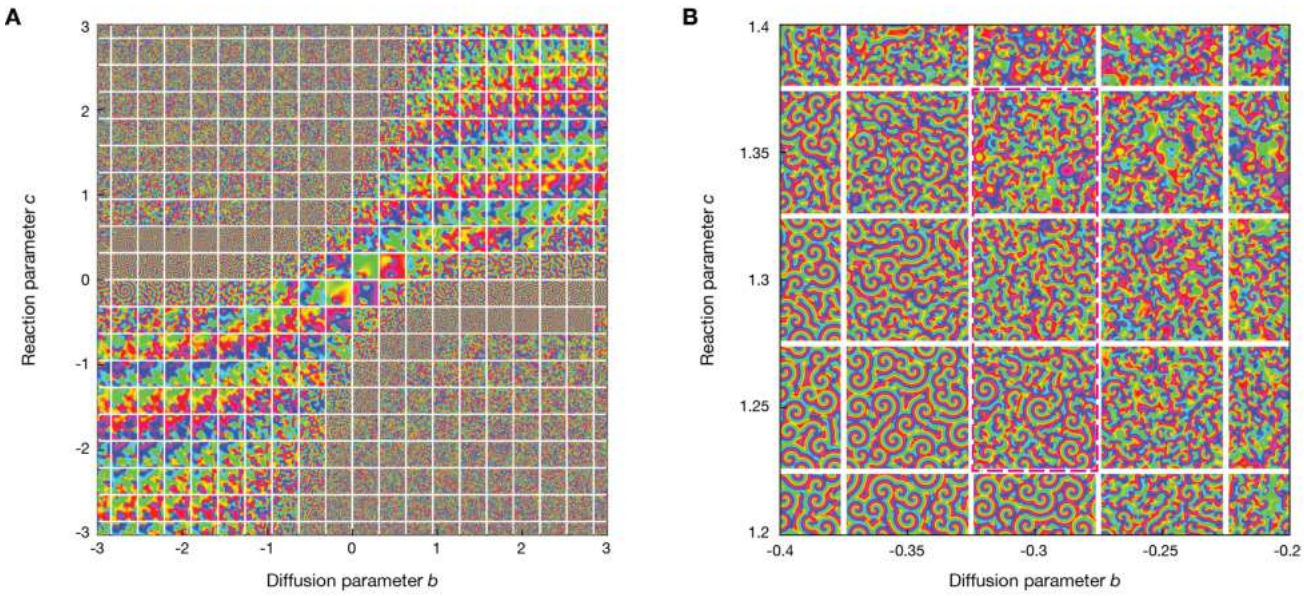

Fig. S6. CGLE atlas. (A) Full phase diagram of dynamic defect patterns in the CGLE. (B) Zoom-in on parameter region matched to experiments.

Derivation of complex Ginzburg-Landau equation and spatiotemporal matching. Following (14, 15), we consider a reaction-diffusion (RD) system

$$\partial_t \mathbf{c} = \mathbf{f}(\mathbf{c}; \boldsymbol{\mu}) + D\nabla_x^2 \mathbf{c} \ ,$$

where $\mathbf{c} \in \mathbb{R}^n$ describes a vector of n dynamical variables, $\mathbf{f} : \mathbb{R}^n \to \mathbb{R}^n$ the local nonlinear dynamics and D the diffusion matrix. When such a system exhibits spatiotemporal oscillations due to undergoing a supercritical Hopf bifurcation as one of the bifurcation parameter μ_i is varied, it has a normal form that is given by the (rescaled) complex Ginzburg-Landau equation (CGLE)

$$\partial_{\tilde{t}}\psi = \psi - (1 + \mathrm{i}c)|\psi|^2\psi + (1 + \mathrm{i}b)\nabla_{\tilde{x}}^2\psi \ ,$$

with a complex amplitude/order parameter $\psi = |\psi|e^{i\phi} \in \mathbb{C}$ as well as linear and nonlinear dispersion coefficients b and c. The CGLE approximates the full RD dynamics by only describing the envelope dynamics of the RD system, which evolve on a slow temporal scale $\hat{t}$ and a coarse spatial scale $\hat{x}$ compared to the original scales t and x. The dynamical variables $\mathbf{c} \in \mathbb{R}^n$ of the full RD system can be approximated with the CGLE amplitude $\psi \in \mathbb{C}$ to first order via

$$\tilde{\mathbf{c}}(\mathbf{x}, t; \boldsymbol{\mu}) = \mathbf{c}_0 + 2\epsilon\sqrt{\sigma_1/|\mathrm{Re}(g)|}\mathrm{Re}\left(e^{\mathrm{i}(\omega_0+\epsilon^2\omega_1)t}\mathbf{u}^{(1)}\psi(\epsilon\sqrt{\sigma_1/\mathrm{Re}(d)}\mathbf{x}, \epsilon^2\sigma_1 t)\right) \ .$$

The oscillation frequency and spatiotemporal scales transform as:

$$\begin{aligned}
\omega_{RD} &= \omega_0 + \epsilon^2\omega_1 + \epsilon^2\sigma_1\omega_{CGLE} \\
\mathbf{x} &= \frac{1}{\epsilon\sqrt{\sigma_1/\mathrm{Re}(d)}}\hat{\mathbf{x}} = \hat{\Lambda}\hat{\mathbf{x}} \\
t &= \frac{1}{\epsilon^2\sigma_1}\hat{t} = \hat{\tau}\hat{t}
\end{aligned}$$

In these mappings, the shortest distance from the Hopf bifurcation is a small parameter $\epsilon = \sqrt{\delta\mu} = \sqrt{||\mu - \mu_{\mathrm{Hopf}}||_2}$. We define the Jacobian matrix $J_{ij} = \partial_{c_j} f_i$. Expanding with respect to ϵ, we define $J(\boldsymbol{c_0}; \mu) \approx J_0 + \delta\mu J_1 \in \mathbb{R}^{n\times n}$. From this matrix J_0 is derived the eigenvector $\mathbf{u}^{(1)}$ as

$$J_0\mathbf{u}^{(1)} = \mathrm{i}\omega_0\boldsymbol{u}^{(1)}$$

with ω_0 the imaginary part of the corresponding eigenvalue. The diffusivity parameter $d = \langle \boldsymbol{u}^{(1)}|D|\boldsymbol{u}^{(1)}\rangle \in \mathbb{C}$. Likewise, $\lambda_1 = \sigma_1 + \mathrm{i}\omega_1 = \langle \boldsymbol{u}^{(1)}|J_1|\boldsymbol{u}^{(1)}\rangle$. To calculate the final parameter g, one must define two higher order matrices $M_{ijk} = \partial_{c_j c_k} f_j$ and $N_{ijkl} = \partial c_j c_k c_l f_i$, with corresponding series expansions

$$\begin{aligned}
M(\boldsymbol{c_0}; \mu) &\approx M_0 + \delta\mu M_1 \in \mathbb{R}^{n\times n\times n} \\
N(\boldsymbol{c_0}; \mu) &\approx N_0 + \delta\mu N_1 \in \mathbb{R}^{n\times n\times n\times n}
\end{aligned}$$

Following this, define

$$\boldsymbol{v}_0 = -2J_0^{-1}M_0\boldsymbol{u}^{(1)}\overline{\boldsymbol{u}^{(1)}}$$
$$\boldsymbol{v}_+ = -(J_0 - 2\mathrm{i}\omega_0\mathbb{1})^{-1}M_0\boldsymbol{u}^{(1)}\boldsymbol{u}^{(1)}$$

from which

$$g = -2\langle\boldsymbol{u}^{(1)}|M_0|\boldsymbol{u}^{(1)}\rangle|\boldsymbol{v}_0\rangle - 2\langle\boldsymbol{u}^{(1)}|M_0|\overline{\boldsymbol{u}^{(1)}}\rangle|\boldsymbol{v}_+\rangle - 3\langle\boldsymbol{u}^{(1)}|N_0|\boldsymbol{u}^{(1)}\rangle|\boldsymbol{u}^{(1)}\rangle|\overline{\boldsymbol{u}^{(1)}}\rangle \in \mathbb{C}$$

Finally, the CGLE parameters are defined in terms of g and d as

$$b = \mathrm{Im}(d)/\mathrm{Re}(d)$$
$$c = \mathrm{Im}(g)/\mathrm{Re}(g)$$

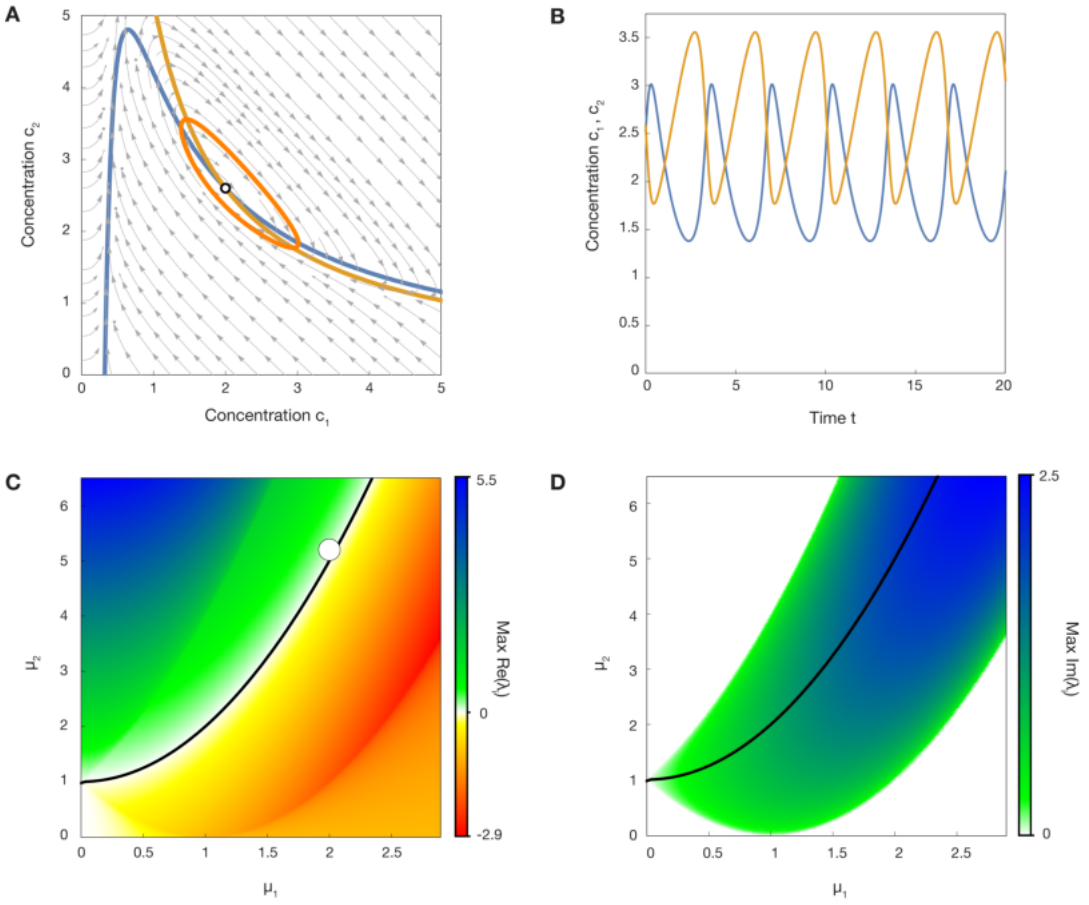

Fig. S7. Brusselator model overview. (A) Phase portrait of the Brusselator model. u- and v-nullclines (blue and yellow) intersect in the unstable fixed point (unfilled circle) encircled by a stable limit cycle (orange). (B) Time series of both dynamical variables u (blue) and v (orange) showing steady nonlinear oscillations over time. (C) Bifurcation diagram of Brusselator model with Hopf bifurcation line (black), where the real parts of both eigenvalues vanish, while the (D) imaginary part is non-zero.

All together, these formula allow a given reaction-diffusion system to be mapped to CGLE near a super-critical Hopf bifurcation. As an instructive example we focus on the explicit CGLE mapping of the Brusselator model, as presented previously in Ref. (14):

$$\partial_t u = \mu_1 - (\mu_2 + 1)u + u^2 v + \nabla_x^2 u$$
$$\partial_t v = \mu_2 u - u^2 v + \delta\nabla_x^2 v$$

The local dynamics of this model are presented in Fig. S7. For $\{\mu_1, \mu_2, \delta\} = \{2, 5.2, 0.7\}$ the corresponding CGLE parameters are $\{b, c\} = \{-0.353, 1.111\}$. Oscillation frequency and spatiotemporal scales obey

$$\omega_{RD} = 2 + 0.1\omega_{CGLE}$$
$$\boldsymbol{x} = 2.92\hat{\boldsymbol{x}}$$
$$t = 10\hat{t}$$

The resulting complex order parameter can be used to approximate the Brusselator to first order as

$$\boldsymbol{c}(\boldsymbol{x},t) = \begin{pmatrix} 2.0 \\ 2.5 \end{pmatrix} + 0.73\,\mathrm{Re}\left(e^{2\mathrm{i}t} \begin{pmatrix} -\mathrm{i} \\ 0.5+\mathrm{i} \end{pmatrix} A(0.34\boldsymbol{x}, 0.1t) \right)$$

The agreement between the full and approximated Brusselator can be seen in Fig. S8.

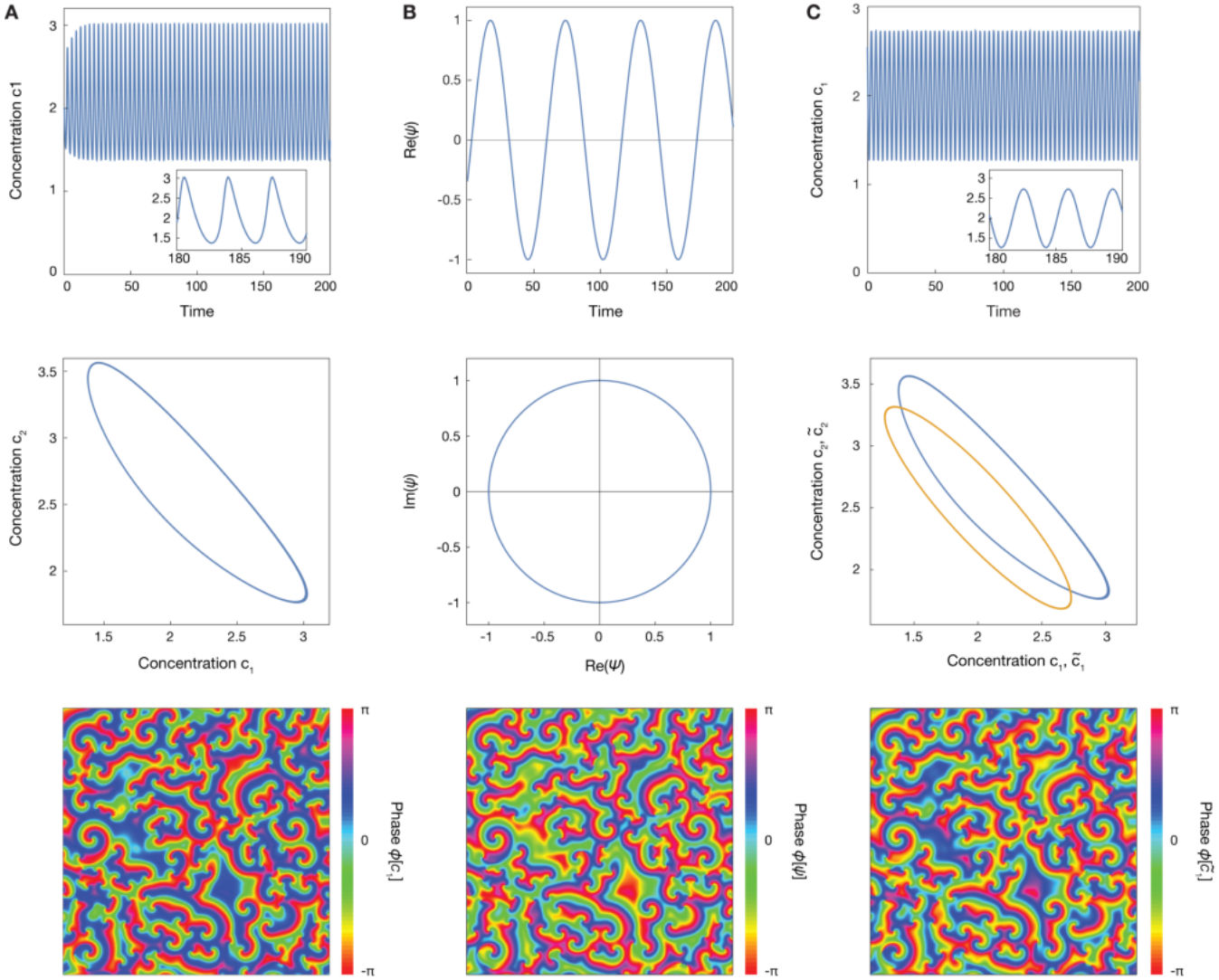

Fig. S8. Comparison of Brusselator, its slow modes described by CGLE and the resulting first order approximation of the Brusselator. (A) Brusselator. (B) Slow mode decribed by CGLE. (C) First order approximation of the Brusselator. In A, B and C, top rows show time series, middle rows phase space dynamics and bottom rows show a snapshot of a 2D spiral gas after 60 Brusselator oscillation periods. All simulations started from topologically identical initial conditions. Temporal and spatiotemporal dynamics agree very well, even though the limit cycles differ. Time interval in all plots covers the same time domain.

For a given value of model parameters b and c, the matching parameters ω_0, $\hat{\Lambda}$ and $\hat{\tau}$ are found as follows. From a (2+1)D spatiotemporal simulation of the CGLE the mean defect density ρ_{CGLE} and speed v_{CGLE} are calculated, along with the local oscillation frequency ω_{CGLE}. The corresponding defect density ρ_{exp}, speed v_{exp} and local oscillation frequency ω_{exp} are calculated for the matching experiment. $\hat{\Lambda} = \sqrt{\rho_{\mathrm{exp}}/\rho_{\mathrm{CGLE}}}$ is chosen so that defect densities are the same between simulation and experiment. To calculate ω_0, we first calculate the dimensionless parameter $\alpha = v_{\mathrm{exp}}\sqrt{\rho_{\mathrm{exp}}}/\omega_{\mathrm{exp}}$, which represents the ratio of slow and fast temporal modes in our system. A corresponding frequency $\omega_{\mathrm{fast}} = v_{\mathrm{CGLE}}\sqrt{\rho_{\mathrm{CGLE}}}/\alpha$ is calculated to be the oscillatory frequency of the fast mode of our matched CGLE system. From this, we acquire $\omega_0 = \omega_{\mathrm{fast}} - \omega_{\mathrm{CGLE}}$. Finally, we chose $\hat{\tau} = \omega_{\mathrm{fast}}/\omega_{\mathrm{exp}}$ to ensure that our systems evolve on the same time scale.

For experimental wave state i, the best-matching CGL model parameters $b = -0.3$ and $c = 1.25$ was determined according to the pattern matching procedures described in Ref. (1). Since wave states i - iii differ only in cellular activity level and protein diffusion parameters are not affected, we fixed the diffusion-related linear dispersion parameter $b = -0.3$ for state ii and iii, and searched the best-matching activity-determining nonlinear dispersion parameter c. To locate the proper c values, we defined an activity constant as the total defect collision

frequency normalized by the mean amount of defects present in field of view (Fig. S9A): $f_0 = \frac{1}{N} \cdot \frac{Z}{\Delta t}$, where Z is the total collision counts over time lapse Δt. We next did a parameter sweep of steady-state CGL slow mode simulations in the activity parameter c with an increment of $\Delta c = 0.01$, returning the growth curve of such collision frequency $f_0(c)$ as a function of c. To directly compare this activity constant in inverse time unit between experiments and CGL simulations, we chose the time unit conversion factor $\gamma(c) = (\omega^{c}_{CGLE}/\omega^{c=1.25}_{CGLE}) \cdot \omega^{c=1.25}_{exp}$, utilizing the prior match of experimental state i with parameter $c = 1.25$. The converted activity constant $\gamma(c) \cdot f_0(c)$ finally gave us the

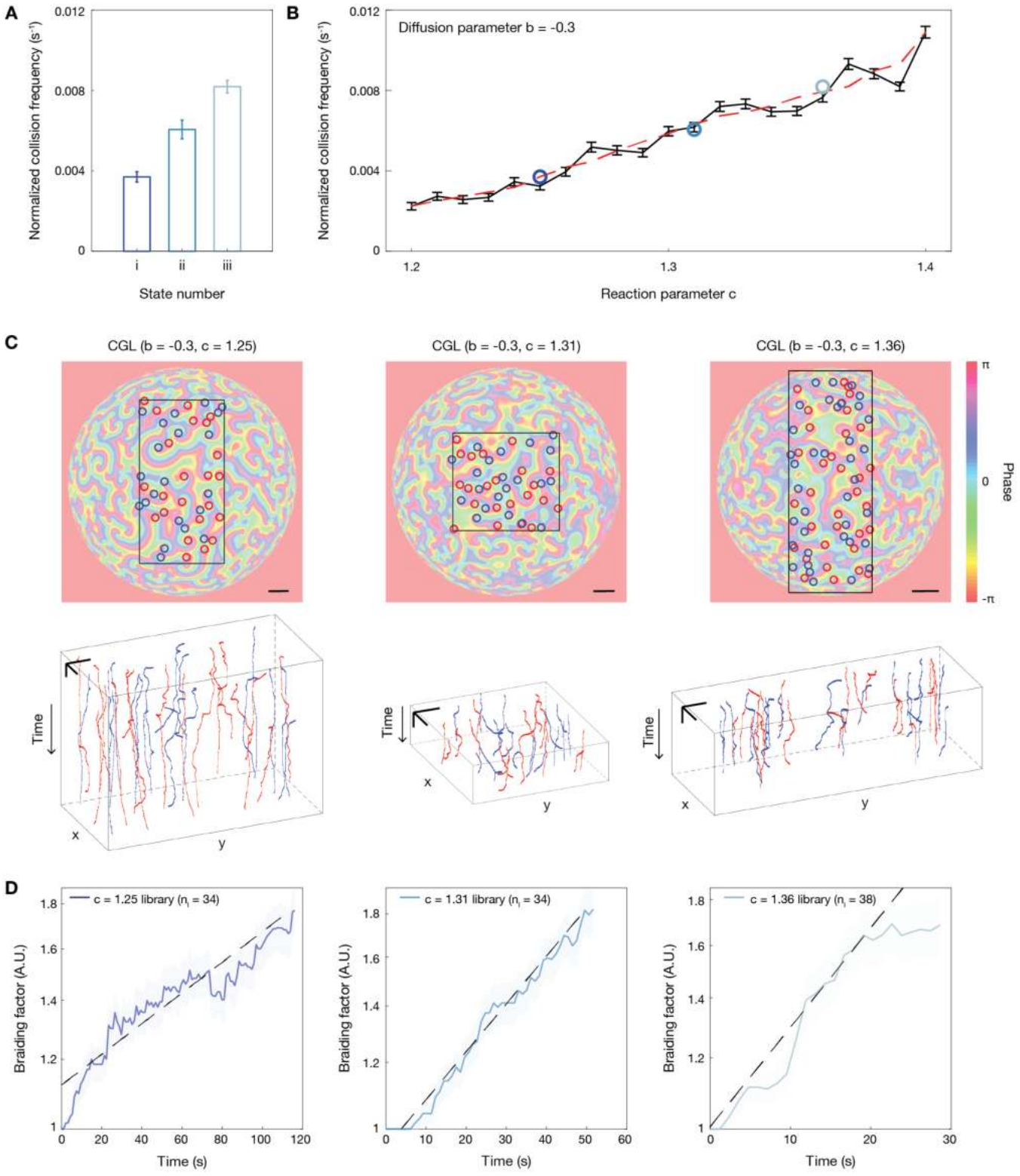

Fig. S9. *(next page)* **Quantifying braiding dynamics of phase defects in complex Ginzburg-Landau simulations.**

Fig. S9. *(preceding page)* **Quantifying braiding dynamics of phase defects in complex Ginzburg Landau simulations.** (A) Normalized collision frequencies for experimental wave pattern state i, ii and iii. (B) Normalized collision frequencies for CGL states simulated with a constant diffusion parameter ($b = -0.3$) and varying reaction parameters. Error bars represent the standard error of normalized collision frequencies across time frames. Circles present the selection of best-matching reaction parameters for state i, ii and iii based on a comparison with the parameter sweep (smoothed, shown as dashed line in red). (C) Libraries of phase defect trajectories constructed with the same experimental observation window across matching CGL simulations for state i - iii. Scale bar: 20 μm; 120 s (vertical) rescaled with CGL-experiment spatiotemporal matching constants. Bottom row: Space-time view of phase defect trajectories consisting of the library for each state. (D) Braiding factor growths calculated for matching CGL simulations for state i - iii. Curves are quantified from the entire library for each state. Shaded regions represent the standard error across reference line projections.

best-matching c values for state ii and iii: $c = 1.31$ for state ii, and $c = 1.36$ for state iii (Fig. S9B). Space-time rescaling constants (Table S2) were then applied for the CGL slow mode simulations for state i - iii to acquire the CGL-experiment phase continuum matching shown in Fig. 4A-C and Movie. S9. Braiding statistics for CGL simulations were also quantified using the space-time rescaled CGL wave states, where the library construction as well as the braiding exponent curve cutoff were executed following the exact same procedures as described in Fig. S4-S5 (Fig. S9C-D).

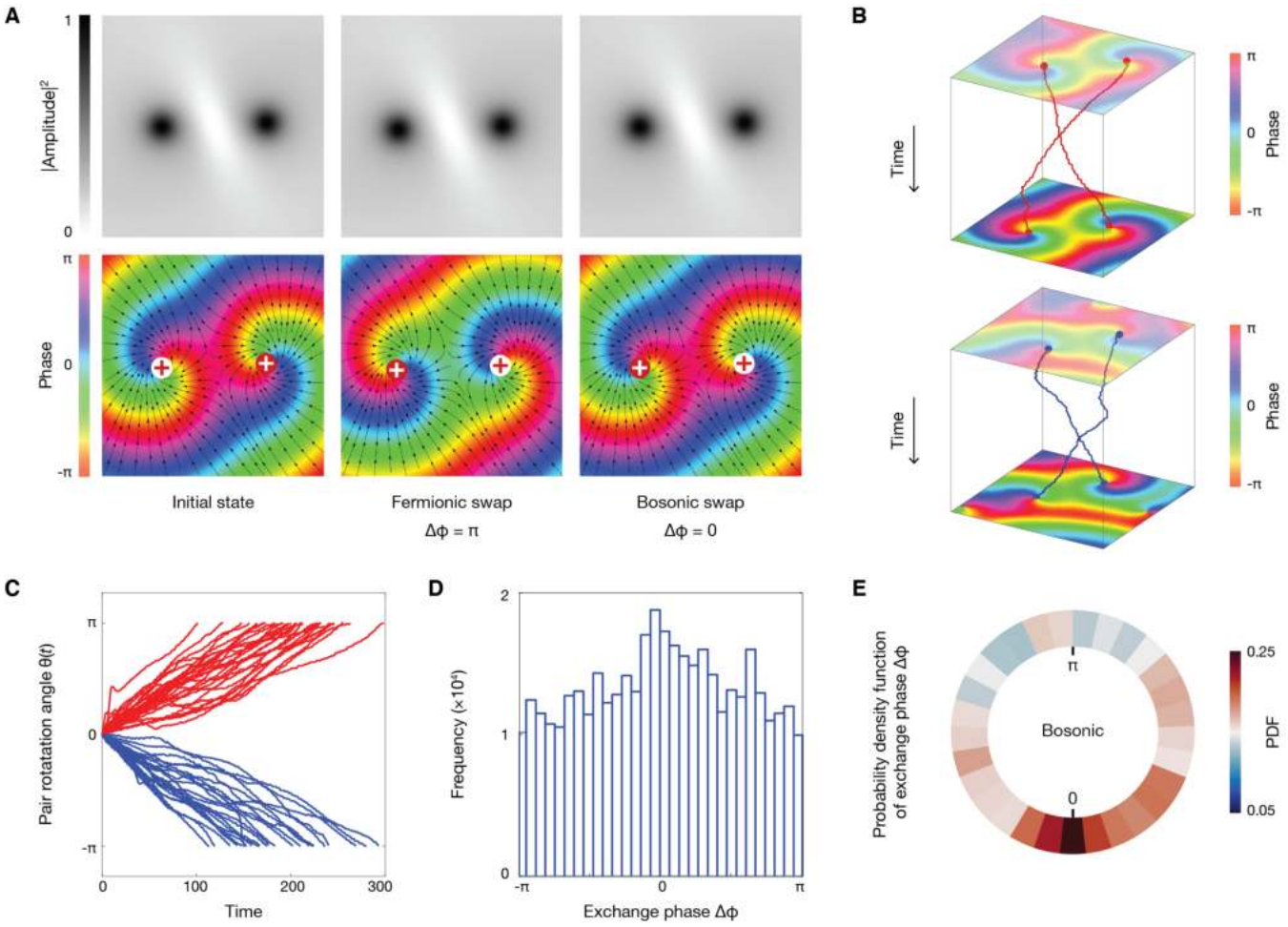

Fig. S10. Pair braiding dynamics of CGL defect pairs and the signature of Bosonic symmetry (A) After completing a counter-clockwise 180° braiding event, the particle positions are exchanged, with initial and final states having matching wave amplitudes (top row). For bosonic excitations, the phase field also returns to the initial configuration (bottom row, right), whereas fermionic states exhibit a global phase shift of π (bottom row, middle). (B) Representative space-time trajectories of persisting plus-plus (left) and minus-minus (right) defect dipoles that spontaneously exhibit large rotations. Shown here are the braiding defect pairs simulated with parameters of experimental state i. (C) Detection of large-rotation defect pairs (N = 83) simulated with parameters of experimental state i. Red curves represent defect pairs with +1 topological charges and blue curves represent those with -1 topological charges. (D) Histogram of exchange phases collected from the large-rotation defect pairs as shown in C. (E) Probability density function of exchange phases collected from the large-rotation defect pairs as shown in C and D.

Quantifying phase exchange symmetry from spontaneous braiding events. The positional exchanges observed in the spontaneous braiding dynamics between same-sign defects inspired us to quantify whether there exists any exchange symmetry for the accompanying phase field. While experimentally observed spontaneous braiding pairs are scarce on account of the chaotic presence of background defects, in CGL simulations we could generate sufficient samples of large-rotation defect pairs. We were interested in calculating the phase shift

$\Delta\phi = \phi(\mathbf{x}_1, \mathbf{x}_2) - \phi^{'}_{\text{exchanged}}(\mathbf{x}^{'}_1, \mathbf{x}^{'}_2)$ for all detectable CGL slow-mode braiding processes. Adopting the definition of exchange symmetries from quantum mechanics, $\Delta\phi$ should have a distribution around 0 (π) if the phase field embeds a Bosonic (Fermionic) exchange symmetry (Fig. S10A).

We acquired the distribution of $\Delta\phi$ using a dataset generated from the slow-mode CGL parameters for experimental wave state i: $b = -0.3, c = 1.25$. The simulation was performed on a plane (since we were interested in small-scale defect dynamics) evolving from a start of randomized initial complex amplitude. To detect large-rotation defect pairs, we dissected each pair of defect dipoles that are nearest-neighbor for a number of consecutive frames, and keep those whose pair rotation angle $|\Delta\theta| = |\cos^{-1}\frac{(\mathbf{x}^{'}_2 - \mathbf{x}^{'}_1)\cdot(\mathbf{x}_2 - \mathbf{x}_1)}{|\mathbf{x}^{'}_2 - \mathbf{x}^{'}_1||\mathbf{x}_2 - \mathbf{x}_1|}|$ exceeds π. The before- and after-braiding frames of phase field $(\phi(\mathbf{x}_1, \mathbf{x}_2), \phi^{'}_{\text{exchanged}}(\mathbf{x}^{'}_1, \mathbf{x}^{'}_2))$ were selected such that the rotation angle $|\Delta\theta|$ matches closest to π within the shortest possible time frames. To account for the fluctuations in defect pairwise distance ($r^{'} = |\mathbf{x}^{'}_1 - \mathbf{x}^{'}_2|$ can be slightly different compared to $r = |\mathbf{x}_1 - \mathbf{x}_2|$) as well as the rotation angle ($|\Delta\theta|$ can be slightly different compared to π), we rotated and rescaled the before- and after-braiding phase field, such that the defect pair's positions perfectly align ($\mathbf{x}^{'rr}_1 = \mathbf{x}^{rr}_2, \mathbf{x}^{'rr}_2 = \mathbf{x}^{rr}_1$). Since pixels were no longer aligned after the rotating-and-rescaling transformation, we interpolated the phase field on the circular region that has a radius $|\mathbf{x}^{rr}_1 - \mathbf{x}^{rr}_2|$ and centers at the defect pair's center of mass. The phase shift $\Delta\phi = \phi^{rr}(\mathbf{x}_1, \mathbf{x}_2) - \phi^{'rr}_{\text{exchanged}}(\mathbf{x}^{'}_1, \mathbf{x}^{'}_2)$ was then taken as a collection of the (interpolated) pixel differences of the transformed and interpolated phase field $\phi^{rr}(\mathbf{x}_1, \mathbf{x}_2)$ and $\phi^{'rr}_{\text{exchanged}}(\mathbf{x}^{'}_1, \mathbf{x}^{'}_2)$, which eventually was used to calculate the $\Delta\phi$ distribution.

Of all 83 large-rotation defect pairs that we extracted from 253 independent CGL simulations, we observe that a typical pair exchange event preserve the local phase field around the pair defects, both for plus-plus defect pairs and minus-minus defect pairs (Fig. S10B). The plus and minus defect pairs exhibit chirality in terms of their spontaneous braiding directions (Fig. S10C). And when the phase shifts distributions were calculated for all 83 large-rotation defect pairs from Fig. S10C, a peak of exchange phase $\Delta\phi$ centered around 0 was observed (Fig. S10D-E), suggesting the existence of a Bosonic phase symmetry in the slow-mode CGL model simulations.

Additionally, we characterized the defect-defect pair scattering dynamics which include simple braiding, virtual pair creation-annihilation and recombination (Fig. 5). As we have demonstrated in the prior study (1), defects accompanying Rho-GTP wave patterns exhibit a disordered phase featuring a low fraction of bound opposite-sign or same-sign defect pairs. To collect effective scattering statistics, we would need (at least) a few tens of events of the same-sign defect pairs that remain bound for long times while far-away from the rest of background defects. Hence the current experimental conditions do not generate enough numbers of scattering events for detailed statistical analysis.

Table S1. Spatial wavelengths and temporal oscillation periods across experimental states i - v.

	Mean of oscillation periods T (s)	Standard deviation of oscillation periods T (s)	Mean of spatial wavelengths λ (μm)	Standard deviation of spatial wavelengths λ (μm)
State i	69.9	2.4	16.58	0.70
State ii	50.0	3.7	15.62	0.62
State iii	49.2	2.9	14.31	0.57
State iv	61.8	3.7	13.72	0.48
State v	69.2	3.8	13.69	0.63

Table S2. Rescaling constants used to match experimental and simulated CGL wave state i - iii.

	$\hat{\tau}$	$\hat{\Lambda}$	ω_0
State i	0.5323	1.6102	1.4304
State ii	0.5159	1.7230	1.6616
State iii	0.5958	2.1483	1.8226

Movie Captions

Movie S1. Propagating waves of Rho-GTP on the surface of an oocyte. Starting from a homogeneous initial state, Rho-GTP spiral waves propagate on membrane and eventually settle into a quasi-steady state ($t > 60$ min). Frame rate is $20\,\mathrm{s}$. Pixel resolution is $0.568\,\mu\mathrm{m}$.

Movie S2. Time-lapse videos of raw and reconstructed Rho-GTP waves recorded in state i. Scale bar: $20\,\mu\mathrm{m}$.

Movie S3. Time-lapse videos of raw and reconstructed Rho-GTP waves recorded in state ii. Scale bar: $20\,\mu\mathrm{m}$.

Movie S4. Time-lapse videos of raw and reconstructed Rho-GTP waves recorded in state iii. Scale bar: $20\,\mu\mathrm{m}$.

Movie S5. Time-lapse videos of raw and reconstructed Rho-GTP waves recorded in state iv. Scale bar: $20\,\mu\mathrm{m}$.

Movie S6. Time-lapse videos of raw and reconstructed Rho-GTP waves recorded in state v. Scale bar: $20\,\mu\mathrm{m}$.

Raw videos in **Movie S2 - S6** are the maximal intensity projections from near-membrane z slices taken with a point-scanning confocal microscope, which were utilized for reconstructing the high spatio-temporal resolution wave patterns (see Methods for details). Raw videos have frame rates of $10-12\,\mathrm{s}$ and pixel resolution of $0.625\,\mu\mathrm{m}$. Reconstructed videos (Methods; fig S2) have a frame rate of $1\,\mathrm{s}$ and pixel resolution of $0.3125\,\mu\mathrm{m}$.

Movie S7. Video of the the space-time structure of the experimental phase field continuum and the trajectories of the embedded topological defects. Scale bar: $5\,\mu\mathrm{m}$ **(space);** $30\,\mathrm{s}$ **(time).**

Movie S8. Time-lapse videos I, II, III and IV of background subtracted raw (see Methods for details) and reconstructed Rho-GTP waves recorded during ATP inhibition drug treatment. Drug was applied in between I and II. Scale bar: $20\,\mu\mathrm{m}$.

Movie S9. Video showing the space-time structure of three-dimensional phase field continuum for experimental wave states i - iii and matching CGL wave states (space-time rescaled). Top row: Phase field evolution in time for CGL wave states (large) aligned with their experimental counterparts (lower-right inset). Middle row: Space-time slices (kymographs) animated at varying slicing positions in space for experimental wave state i - iii. Bottom row: Space-time slices (kymographs) animated at varying slicing positions in space for CGL wave states matched and rescaled for i - iii. Scale bar: $20\,\mu\mathrm{m}$ **(space);** $50\,\mathrm{s}$ **(time).**

Movie S10. Time-lapse videos of representative small-scale defect pair-scattering events that happen spontaneously both in experimental and matching CGL wave states: Simple braiding event, virtual particles' pair creation/annihilation event, and recombination event. Simulated CGL wave states were space-time rescaled to align with experimental wave states. Example defect pairs are the same as shown in Fig. 4A-C snapshots. Scale bar: $10\,\mu\mathrm{m}$.

References

1. TH Tan, et al., Topological turbulence in the membrane of a living cell. *Nat. Phys.* **16**, 657–662 (2020).
2. HA Benink, WM Bement, Concentric zones of active RhoA and Cdc42 around single cell wounds. *J. Cell Biol*. **168**, 429–439 (2005).
3. WM Bement, et al., Activator–inhibitor coupling between Rho signalling and actin assembly makes the cell cortex an excitable medium. *Nat. Cell Biol.* **17**, 1471–1483 (2015).
4. J Bischof, et al., A cdk1 gradient guides surface contraction waves in oocytes. *Nat. Commun.* **8**, 849 (2017).
5. MC Wigbers, et al., A hierarchy of protein patterns robustly decodes cell shape information. *Nat. Phys.* **17**, 578–584 (2021).
6. F Niiya, T Tatsumoto, KS Lee, T Miki, Phosphorylation of the cytokinesis regulator ECT2 at G2/M phase stimulates association of the mitotic kinase Plk1 and accumulation of GTP-bound RhoA. *Oncogene* **25**, 827–837 (2006).
7. JP Boyd, *Chebyshev and Fourier Spectral Methods*. (Courier Corporation), (2001).
8. JC Mason, DC Handscomb, *Chebyshev Polynomials*. (CRC Press), (2002).
9. M Frigo, S Johnson, The Design and Implementation of FFTW3. *Proc. IEEE* **93**, 216–231 (2005).
10. L Marple, Computing the discrete-time "analytic" signal via FFT. *IEEE Trans. Signal Process*. **47**, 2600–2603 (1999).
11. C Arias Abad, Introduction to Representations of Braid Groups. *Rev. Colomb. de Mat.* **49**, 1–38 (2015).
12. M Budišić, JL Thiffeault, Finite-time braiding exponents. *Chaos* **25**, 087407 (2015).
13. A Townsend, H Wilber, GB Wright, Computing with Functions in Spherical and Polar Geometries I. The Sphere. *SIAM J. Sci. Comput*. **38**, C403–C425 (2016).
14. Y Kuramoto, *Chemical Oscillations, Waves, and Turbulence*. (Springer) No. 19, (1984).
15. M Ipsen, L Kramer, PG Sørensen, Amplitude equations for description of chemical reaction–diffusion systems. *Phys. Rep.* **337**, 193–235 (2000).